

# Astrometric calibration and source characterisation of the latest generation neuromorphic event-based cameras for space imaging

Nicholas Owen Ralph (✉), Alexandre Marcireau, Saeed Afshar, Nicholas Tothill, André van Schaik, and Gregory Cohen

*International Centre for Neuromorphic Systems, MARCS Institute for Brain, Behaviour and Development, Western Sydney University, Kingswood 2747, NSW, Australia*

## ABSTRACT

As an emerging approach to space situational awareness and space imaging, the practical use of an event-based camera (EBC) in space imaging for precise source analysis is still in its infancy. The nature of event-based space imaging and data collection needs to be further explored to develop more effective event-based space imaging systems and advance the capabilities of event-based tracking systems with improved target measurement models. Moreover, for event measurements to be meaningful, a framework must be investigated for EBC calibration to project events from pixel array coordinates in the image plane to coordinates in a target resident space object's reference frame. In this paper, the traditional techniques of conventional astronomy are reconsidered to properly utilise the EBC for space imaging and space situational awareness. This paper presents the techniques and systems used for calibrating an EBC for reliable and accurate measurement acquisition. These techniques are vital in building event-based space imaging systems capable of real-world space situational awareness tasks. By calibrating sources detected using the EBC, the spatiotemporal characteristics of detected sources or “event sources” can be related to the photometric characteristics of the underlying astrophysical objects. Finally, these characteristics are analysed to establish a foundation for principled processing and observing techniques which appropriately exploit the capabilities of the EBC.

## KEYWORDS

neuromorphic  
event-based camera (EBC)  
space imaging  
space situational awareness  
(SSA)  
astronomy

## Research Article

Received: 31 March 2023

Accepted: 18 May 2023

© The Author(s) 2023

## 1 Introduction

The Earth’s orbit is a vantage point for many commercial, scientific, and defense satellites. High-demand orbital slots are increasing rapidly and thereby, increasing the likelihood of collisions resident space objects (RSOs) [1]. The proliferation of Earth’s orbit requires an effective approach to space situational awareness (SSA) to mitigate these hazards by gathering information in the space environment to coordinate satellite operations. Optical space imaging approaches for SSA are commonly used for observing extra-atmospheric objects such as satellites and astrophysical objects [2]. Recently, event-based camera (EBC), a novel class of imaging devices, was demonstrated as an alternative and new approach in

space imaging and SSA without many of the constraints of typical frame-based imaging sensors such as charge-coupled devices (CCDs) and complementary metal-oxide semiconductors (CMOSs)-based active pixel sensors (APSS) [3].

The EBC is a biology-inspired class of vision sensors that drew inspiration from the photoreceptors in biological eyes. This inspiration is based on the mechanisms that provide the retina with remarkable capabilities [4], namely, the manner in which the retina extracts and efficiently encodes meaningful information from a visual scene [5]. Each pixel in the EBC contains an analog circuit that operates as a contrast detector. Each pixel is also independent and asynchronous from the

✉ N.Ralph@westernsydney.edu.au

others and emits data only when a positive or negative contrast variation is detected.

Because these sensors detect variations in contrast rather than integrating the light at each pixel, the pixels have an exceptionally high dynamic range. Furthermore, the independent characteristic of each pixel enables the sensors to search for variations around their own set points. This prevents the saturation problems caused by fixed-time integrating cameras [7]. This pixel-level variation causes these sensors to produce data that are fundamentally different from the output of a conventional camera [8], as shown in Fig. 1. Rather than frames, these devices output a stream of variation events with a microsecond resolution. The output of these sensors is also activity dependent. This enables them to produce significantly less data than conventional cameras for sparse scenes. Combined with their large dynamic range, these sensors are exceptionally well suited for space

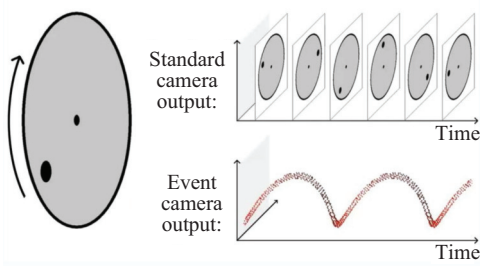


**Fig. 1** Response of an EBC to a rotating dot stimulus, which produces a continuous stream of events with a high temporal resolution. Using a frame-based imaging system, discrete image frames would rather be produced in discrete sample intervals, which are more vulnerable to blur effects. Reproduced with permission from Ref. [6], © The Author(s) 2018.

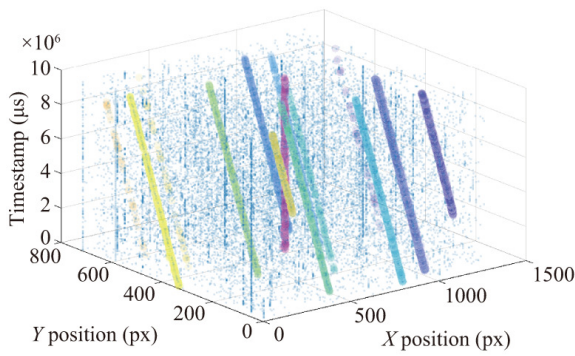
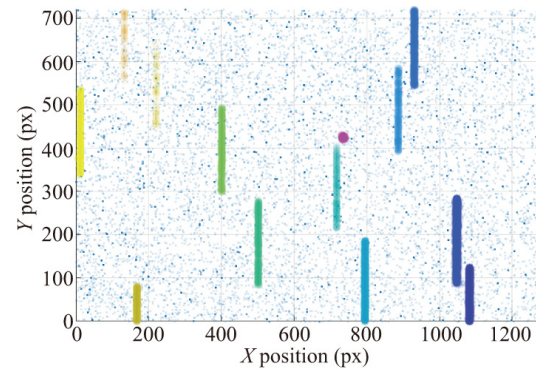


**Fig. 2** Labelled 10 s Gen 4 HD asynchronous time-based imaging system (ATIS) observation of MEO BEIDOU-3 M1 (NORAD ID 43001) (magenta) in the 3D spatiotemporal event-stream (left) and a 2D event accumulation using standard mount tracking (right). Background stars appear among the background noise as streaks moving through the FOV (color overlay given by target label).

imaging applications. A typical event-stream output of an RSO observation using the advanced Gen 4 HD ATIS is shown in Fig. 2.

The EBC was demonstrated successfully as a new approach to SSA and space imaging [3]. In this study, an event-based (EB) telescopic space imaging system was demonstrated to be capable of observing RSOs in low Earth orbit (LEO) and geostationary Earth orbit (GEO). In these experiments, the EB space imaging system performed with a significantly higher temporal resolution and lower output data volume than conventional CCD sensors (which require longer exposure time and display blur effects when observing moving targets).

Dedicated RSO tracking algorithms for EB vision data have been established using frame-based [9] and EB [10] representation and processing techniques. RSOs and aircraft have been observed using EBCs in various conditions and optical setups [11]. Frame-based star trackers have also been developed to transform EB pixel measurements into world-coordinate frames using astrometric calibration. This so-called “star mapping” has been performed using integrated event-frames with manual motion compensation [12], frame generation using a basic form of contrast maximization [13], and motion compensation using Hough line detection [14]. EB datasets were developed in these studies with hand-labelled real-world tracking data [9, 10] and physically simulated astrophysical sources [13, 14]. The space-based operation of the EBC for spacecraft landing on the Moon was investigated using simulated data [15]. The use of the EBCs for satellite characterization has also been studied [16]. The viability of EBC operation in the high-



radiation environment of LEO was tested using a physical simulation [17]. Here, the authors concluded that EBC is robust to on-orbit operation in the presence of neutron radiation.

The viability of the EBC was assessed in Refs. [18] and [19]. These studies discussed the limitations and advantages of EBC. They concluded that although less sensitive than comparatively integrated CCD sensors, EBC represents a new potential avenue for space imaging given its inherent high time resolution, low latency, and low volume data output. In particular, Ref. [19] evaluated the EBC and performed a large sky survey using a third-generation EBC (further details on EBC are provided in Section 2). In this work, we established a model for the limiting magnitude of third-generation EBCs. It is empirically evaluated by observing stars while simultaneously tracking. The authors also evaluated the limiting magnitude of the EBC at varying angular scan rates. This work concluded that the EBC shows significant potential for small-aperture, large-field persistent SSA in terms of their “efficient capture of temporal information”. A model of the EBC was also developed to simulate EB data for SSA [20]. Herein, a physics-based end-to-end model for the EB sensing of RSOs was proposed. This model was designed to function as a tool to advise system design decisions for the SSA and to provide a consistent simulated output for algorithm development with EBCs. A simulator similar to that proposed in Ref. [21] generated simulated RSO observations to develop and evaluate an EB tracking algorithm for the SSA. These works were based on third-generation EBCs; however, recently, the Prophesee “Gen 4 HD” EBC has been made available with significant improvements in performance, as detailed in Table 1.

The overall goal of SSA operators is to provide fast, accurate, and reliable information on the RSOs. The characteristics of EB space imaging systems are well-suited to these goals. The high temporal resolution and low latency of EBC enable an EB imaging system to rapidly observe targets in addition to responding rapidly

to new and unexpected RSOs. The low output data volume produced by the EBC is attractive for SSA operators because it reduces the power, storage, and cost requirements of conventional ground- and space-based SSA networks. It is vital to reduce these requirements and facilitate an increased RSO tracking capacity as data collection efforts increase in response to the rapidly growing RSO population.

EB sensing systems represent a potentially disruptive technology for conventional imaging and particularly space imaging. Few studies have been conducted on the observation limits of the EBC, the spatiotemporal characteristics of event sources, their relationship with target photometric properties, and how these characteristics vary while observing at varying angular mount scan speeds. Night-sky limiting magnitudes were verified independently as magnitude 10.38 in Ref. [18] using third-generation dynamic vision sensor (DVS) with 320 ms-duration event accumulation frames at a  $1 \times$  sidereal rate, and magnitude 5.45 while performing a scanning slew at  $300 \times$  sidereal rate. Similar limits were observed in Ref. [3] using the same sensors at a magnitude of 10.19 at  $1 \times$  sidereal tracking with smaller aperture telescopes. The most detailed study of the spatiotemporal characteristics of source observations is Ref. [19]. The authors established a model for the limiting magnitude of third-generation ATIS and DVS EBCs. These were evaluated empirically by observing stars while simultaneously tracking. The authors proposed a theoretical limit of 9.6 in these evaluations and observed a limiting magnitude of 9.8 using relatively small-aperture telescopes. In addition, the limiting magnitude of the EBC at varying angular scan rates indicated that no sources could be detected at 0.5 deg/s. The authors noted that the empirical limiting magnitude reduced by approximately 1.5 magnitudes as the scan rate increased from 0.01 to 0.1 deg/s. Additionally, the event rate of a source increased rapidly as the apparent brightness increased.

**Table 1** Specifications and comparison of an early generation Inivation DVS364 and the next-generation Prophesee Gen 4 HD ATIS EBC used in this study [7]

Camera	Resolution (px)	Latency (μs)	Dynamic resolution (dB)	Minimum contrast sensitivity (%)	Chip size (mm <sup>2</sup> )	Pixel size (μm <sup>2</sup> )	Fill factor (%)
DVS346	346 × 260	20	120	14.2–22.5	8 × 6	18.5 × 18.5	20
Gen 4 HD	1280 × 720	20–150	> 124	11	6.2 × 3.5	4.86 × 4.86	> 77

Although EBC has demonstrated clear advantages as a new and complementary approach to SSA and space imaging, it is difficult to develop algorithms for processing these novel data. To obtain functional RSO state estimates using EB data, precise position and timing information should be gathered from a space imaging system to convert event measurements in the pixel frame to a standard world coordinate frame. A real-time online EB RSO tracking system that sufficiently leverages the capabilities of the EBC and can produce calibrated, accurate, and precise state estimations of the RSO has not been published. An in-depth analysis of the relationships between the spatiotemporal features and the photometric characteristics of faint point sources and bright extended sources at varying scan rates and different observation conditions has not been conducted. Additionally, the Gen 4 HD, as the latest and currently best-performing EBC for SSA, has not been assessed in a similar manner.

In this study, the first extensive and pure EB star catalogue analysis was developed and analyzed using real-world data. The study captured the limitations of EBC in addition to the complex spatiotemporal features and characteristics of sources observed using the Gen 4 HD EBC at different scanning rates, observation conditions, and weather conditions. The first automatic star mapper using only real-world EB observations was developed to conduct this analysis. By analyzing the EB features of each event source and their relationship with the underlying photometric characteristics of the associated source, future examination of EB data processing systems and algorithms can be based on a more robust understanding of EB target-measurement dynamics and EB space imaging limitations.

## 2 Methodology and data collection

This analysis was conducted on a dataset of real-world observations containing constant-speed slews through a series of dense star fields using the Gen 4 HD at Astrosite-2. The Astrosite mobile observatories were constructed from standard 20 ft shipping containers, each with a control and telescope room. The mount and lifting mechanism are installed in the telescope compartment, where the lift lifts the telescope mount out of the container via a retractable ceiling during observation (as shown in Fig. 3). Astrosite operations can be performed remotely or in the control room. As a mobile platform,

astrosites can be shifted rapidly to new observation sites to alter the total effective coverage area, also known as field of regard (FOR). Because telescope-mount lifting mechanisms and the container are neither sufficiently rigid nor built into a structural foundation, astrosite imaging systems are more vulnerable to movement and instability during observation than observatory-based telescopes. However, the high temporal resolution of EBC allows for the compensation of this motion without the blurring effect induced by the motion on conventional cameras. Furthermore, because EBC is a contrast-based detector, the additional mutual motion caused by vibrations and instability can increase the contrast in the scene.

Astrosite-1 is a first-generation astrosite observatory. It contains the Software Bisque Paramount ME II equatorial mount supported by a pneumatic scissor lift. Astrosite-1 is outfitted with an Officina Stellare RH200, which has 200 mm aperture, 600 mm focal length, and effective field-of-view (FOV) of  $35.52 \times 20.05$  arcsec with a Gen 4 HD EBC. Astrosite-2 is a second-generation mobile observatory. The imaging system comprises a Planewave L600 Alt-Az mount on a pneumatic lift sturdier than Astrosite-1 and is equipped with an identical telescope. The specifications of the mounts at each astrosite are listed in Table 2.

This variable-speed EB observation dataset<sup>①</sup> comprises 11 observations per field for a duration of 10 s each, with slew speeds decreasing from 0.5 deg/s (or a 1200% sidereal rate) by 50% to a minimum of 0.00048 deg/s (or a 11.5% sidereal rate). Here, the sidereal rate is given as 0.00418 deg/s.

Four fields were observed. Each of these was centered on a single bright source (approximately magnitude 0) among a dense star field with a variety of brightness to maximize the source diversity. This is shown in Fig. 4 and summarized in Table 3. At the start of the observation, the mount was slewed through the target field only on the azimuthal axis (for a smooth mount motion). It reached the center at the approximate midpoint of the recording. In the case of the slowest slews, the recording began with the source near the center of the FOV (given the time required to move the mount at a sidereal rate of 11.5% to transit the FOV).

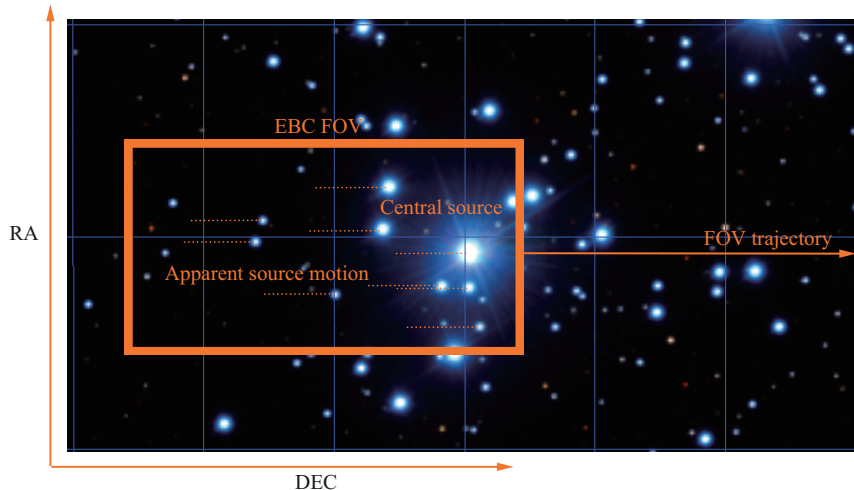
<sup>①</sup>The Event-Based Space Imaging Slew Speed Dataset is available from [https://github.com/NicRalph213/ICNS\\_NORALPH\\_Event-Based-Space\\_Imaging-Speed\\_Dataset](https://github.com/NicRalph213/ICNS_NORALPH_Event-Based-Space_Imaging-Speed_Dataset).

**Table 2** Telescope mount configuration in Astrosite-1 and Astrosite-2

Astrosite	Telescope mount	Design	Maximum speed (deg/s)	Pointing accuracy (arcsec)	Mount tracking accuracy (arcsec)
Astrosite-1	Software Bisque Paramount MEII	Equatorial	4	< 30	~1
Astrosite-2	Planewave L600	Altazimuth	50	< 10	< 0.3

**Table 3** Summary of each field in publicly available speed survey dataset collected using Astrosite-1 comprising 11 observations per field for a duration of 10 s each, with slew speeds decreasing from 0.5 deg/s (or a 1200% sidereal rate) by 50% to a minimum of 0.00048 deg/s (or a 11.5% sidereal rate)

Field ID	Field centre	Central source	Central source magnitude
0	191.930378, -59.688764	Mimosa HIP 62434	1.25
1	125.628542, -59.509483	Avior HIP 41037	4.2
2	144.302803, 6.835782	10 Leo HIP 47205	5.0
3	182.103152, -24.728782	Alchiba HIP 59199	4.0

**Fig. 3** (a) Astrosite-1 and (b) Astrosite-2 at the Werrington North Campus, NSW, Australia.**Fig. 4** Demonstration of the speed survey observations with the apparent motion of the EBC FOV against a background star field (Jewel Box, NGC 4755) during a constant speed declination axis (DEC) slew. Star field generated using Stellarium.

Using a field velocity estimator, the event stream was motion-compensated for the scanning slew motion of the mount to collapse the observed event streaks into event sources in a global “star map” frame where the

sources resemble their apparent static appearance. The relative positions of the event sources could be used to perform astrometric calibration of the field. The astrometric calibration functioned as an estimate of the

transformation between the pixel and world frames. This transformation was used to identify the sources on the star map using an established optical sky survey. Finally, the photometric and physical characteristics of the real-world surveyed sources were related to the spatiotemporal features and characteristics of the sources in the star map. This analysis aimed to evaluate the following:

- (1) effect of slew rate on the spatial distribution, extent, and event rate of an event source;
- (2) accurate measurement methods for source centroid and spatiotemporal features of an event source;
- (3) differing spatiotemporal features and dynamics of point sources and extended sources;
- (4) dynamics introduced by varying wind and sky observation conditions;
- (5) limitations and trade-off between varying mount slew rates and the detectable contrast of sources.

The analysis is conducted in three steps: firstly, star maps are created from the event streams. The second step is to detect and localize sources within the star map. The third step is the astrometric calibration of the star map. It is critical to resolve these challenges for converting the centroid measurements of the RSOs in pixel coordinates into world coordinates to perform real-world SSA tasks.

### 3 Creating star maps from event data

A star map is an image of a source or a table of source positions observed from a space imaging system. An event star map is an image frame that compensates for the motion of the mount and contains spatiotemporal features of sky sources. In these frames, the stars and astrophysical objects appear as fixed points. Producing a star map of event data enables the analysis of the spatial features of these event sources and provides an avenue for performing astrometric image calibration on event data using established techniques. This image calibration facilitates the identification of astrophysical sources by extracting static source positions from the moving field and comparing their relative geometric arrangements with known surveyed star positions.

Consider a star field observation collected using an EB space imaging system. The sensor tracks siderally and is stationary with respect to a stellar source, whereas the pixel projections of these sources on the celestial sphere are static. In this case, event sources appear as static and condensed blob-like features, with contrast produced only

by atmospheric effects. While undergoing a nonsidereal translation, such as an angular slew, these stellar sources translate and appear with a higher contrast owing to the mutual motion of the mount. In this case, the angular slew motion of the mount is a rotation projected onto a local tangent plane on the celestial sphere. This causes the sources to appear as streaks translating within the image frame and spatiotemporal event stream. When tracking the RSO, background sources appear as streaks. Simultaneously, the mount is centered on the moving target, which resembles a stationary source as shown in Fig. 2. Two “field velocities” are present in this scenario: one for the background sources and the other for the tracked target. If compensated for by the target’s motion, the target would appear stationary, whereas other sources would appear as streaks. If the background sources are compensated for, the target appears as a streak, and the background sources appear as static and condensed event sources. To accurately understand the position of the RSO with respect to the background sources during mount tracking, a system for star map generation and background field velocity compensation should be designed.

Event star map images can be generated by compensating for one of the field velocities in the EB observation. By transforming or “warping” events by the inverse of the translation velocity, the event streaks are collapsed along their trajectory into features that resemble a spatial estimate of the underlying source’s point spread function (PSF). These event sources comprise an event star map. Calculating the motion-compensated position  $e'_k$  of an event  $e_k$  by warping on a star map is trivial and can be simplified using the constant-field velocity hypothesis  $\theta_v = V = [v_x, v_y]^T$  to develop a single star map frame. This is particularly true for the speed dataset, where the mount slews at a constant velocity. Consider the event stream  $\mathcal{E}$  comprising a set of individual events,  $e_k$  with a pixel position on the image plane  $x, y$  at time  $t$  and contrast polarity  $p$ :

$$e_k = (x, y, t, p) \quad (1)$$

Using notations similar to those in Ref. [22], the warped event  $e'_k$  is a function of the velocity hypothesis  $\theta_v$  (the field velocity  $V$  in this constrained star mapping case) at a reference event timestamp  $t_k$ :

$$e'_k = W(e_k, t_k; \theta) \quad (2)$$

In this constrained case, the star map

$$\mathbf{e}'_k = \begin{bmatrix} x'_k \\ y'_k \end{bmatrix} = \begin{bmatrix} x_k \\ y_k \end{bmatrix} - \begin{bmatrix} v_{x_k} \\ v_{y_k} \end{bmatrix} (t_k - t_0) \quad (3)$$

The star map image frame of the warped events  $H$  can then be calculated using  $N_e$  events from the event stream and known warping hypothesis.

$$H(e_k; \theta) = \sum_{k=1}^{N_e} b_k \delta(e'_k) \quad (4)$$

where  $b_k$  is the accumulated value of the warped events if these are warped onto the same projected pixel region ( $\delta$ ). In this experiment, star maps with and without negative polarity events ( $b_k = p_k$ ) and without negative polarity events ( $b_k = 1$ ), respectively, were analyzed.

Event warping and motion compensation using EBC have been studied well for conventional applications, with the field velocity estimation method as the distinguishing factor between each study. The contrast maximization approach is the most widely used. Herein, the point trajectories in the event stream are estimated by maximizing an objective function  $f(\theta_v)$  to produce a set of suitable warping parameters  $\theta_v$ . The most common approach for estimating the warping parameters is to use the pixel value variance of the warped image [22] and the maximum accumulation of pixel values on the warped image [23].

A detailed review of these objective functions was presented in Ref. [24]. Various optimization approaches have been examined to locate the optimal  $\theta_v$ , including gradient ascent [23], branch-and-bound [25], random sample consensus (RANSAC) optimization [26], and gradient descent using neural networks [27].

Although generic event warping and motion compensation have a strong foundation in the EB literature, few studies have focused on space-based applications. In Ref. [12], a star map was generated using basic motion compensation with Eq. (3) on real-world space imaging data using manual field-velocity estimation. Algorithms for automatically calculating the field velocity to generate star maps have been developed using the contrast maximization technique [13], in addition to motion compensation by estimating the field velocity using target tracking with Hough line detection [14]. Both Refs. [13] and [14] employed physically simulated data. In Ref. [19], integrated event frames were used rather than star maps for the analysis and astrometric calibration. Rather, conventional images

are co-collected using CMOS, with the scanning-mode observations astrometrically calibrated by calibrating the conventional image and then correlating the calibrations with the event frame. These studies produced star maps capable of astrometric calibration. However, no study has been published that uses an automatic algorithm to estimate the field velocity to generate star maps using real-world data.

This study solved the field-velocity estimation problem from an alternative and simplified tracking perspective. Because all the background sources in a field are static on the celestial sphere, these exhibit constant apparent motion consistent with constant-slew motion. The observations in the dataset used in this study reveal a constant motion and a significantly bright source that transits the FOV in the middle of the recording. Using these constraints, the field velocity can be calculated as the highest-likelihood single-target measurement association hypothesis for the largest target using a basic global nearest neighbor (GNN) single target tracking (STT) state estimator. This approach is similar to Ref. [28], where the so-called “leap-frog observation” was used to constrain the tracking task to a more simple STT task. A GNN style tracker was selected as the most fundamental first principles tracker with capabilities suited for this tracking a conveniently detectable and bright single target with a constant linear motion measured in short intervals. Other similar Bayesian trackers such as joint probabilistic data association (JPDA) [28], multiple hypothesis tracker (MHT) [9], and Gaussian mixture probability hypothesis density (GMPHD) [29] are designed to track an unknown and varying number of targets with complex motion. These are not required for this tracking task. Using a GNN tracker, the global single-target track hypothesis is given by the state  $x_k$  of the clustered source in the source set  $\mathcal{X}$  at time-step  $k$ . The largest extent  $E$  in the FOV is given by

$$x_k = \mathcal{X}_k^{\text{argmax}(E)} \quad (5)$$

The field velocity  $\theta_v$  is given by the position state variation of the largest source between time intervals as Eq. (6):

$$\theta_v = \frac{x_k - x_{k-1}}{t_k - t_{k-1}} \quad (6)$$

Using this single global hypothesis, the field velocity of the observation segments can be estimated with a

reasonable accuracy by assuming that the state velocity estimate of the largest target at each event time-step is constant for the observation duration. As shown in Algorithm 1, multiple frames are processed by the STT within 3 s before and after the midpoint of the observations. Each has an integration time listed in the integration time of the velocity estimation frame, which accumulates at the velocity estimation frame interval. The frame integration time and intervals used by STT are listed in Table 4. Here, slower fields require longer frames for an accurate tracking. The integration time for the star maps is 3 s for all the fields and slew speeds. The final field velocity is calculated as the mean target velocity of the largest target over all the intervals. The outlier-velocity-estimates beyond three mean signals were filtered. Using the STT-estimated field velocity and assuming that this velocity is constant throughout the observation period, a star map can be generated by warping the event stream accordingly. Detecting event

---

**Algorithm 1** STT motion estimator

---

```

return Star map from mean field velocity
estimate,  $\theta_v$  of event stream  $\mathcal{E}$  over star map
integration  $H_t$ 
while Event stream  $\mathcal{E}$  is not empty do
    for event frame integration  $I_i$  with inter-frame
    interval time  $T_g$  do
        detect largest object state  $x_k = \mathcal{X}_k^{\text{argmax}(E)}$ ;
         $\theta_v^k = \Delta x_k / \Delta l_k$ ;
        append  $\theta_v^k$  to hypothesis list  $\theta_N$ ;
        update global  $\theta_v = \text{mean}(\theta_N)$ ;
    end for
    for event  $e_k$  from event stream  $\mathcal{E}$  for duration
     $H_t$  at  $\mathcal{E}$  midpoint do
         $e'_{xk} = x_k - \theta_{vx} \Delta l$ ;
         $e'_{yk} = y_k - \theta_{vy} \Delta l$ ;
        integrate warped  $e'_k$  into warped frame  $H$ ;
    end for
end while

```

---

sources in a star map for astrometric calibration and spatiotemporal feature analysis still requires a source-finding algorithm to accurately localize event sources within the star map.

## 4 Localizing and analyzing event sources in the star map

Astronomical source finding is the process of locating and identifying sources as Gaussian PSFs on the image plane among background noise [30]. Typically, source finding is performed using statistical techniques such as image sigma-clipping to isolate the source PSFs from the background noise. In the star mapping and calibration pipeline developed in this study, sources were detected in a sigma-clip-filtered star map using a density-based clustering algorithm, density-based spatial clustering of applications with noise (DBSCAN), and the pixel connectivity. Because the star mapping process produces an accumulated event frame, frame-based techniques similar to those in conventional astronomy can be performed. Clustering algorithms such as DBSCAN can be used on event data to cluster spatial characteristics (as is the case in conventional imaging). However, DBSCAN can also be clustered based on the temporal characteristics using the associated timestamps of each compensated event in the frame. Performing higher-dimensional clustering using temporal source information improves source clustering by preventing spurious associations between events with high spatial and low temporal similarities.

The commonly used sigma-clipping method was implemented in this study to filter regions in the event star maps. Sigma-clipping is a conventional technique in astronomical signal processing. Here, values in a set with a target numerical characteristic are removed or “clipped” if the characteristic value lies outside a standard deviation boundary from the global mean of the set (example in Ref. [31]). This process is iterated until a stopping

**Table 4** Integration time for the individual accumulated frames used by the STT to estimate the field velocity and compose the star map. The fields and slew speeds use identical velocity and star map integration time

Speed range (deg/s)	Velocity estimation frame integration time (s)	Velocity estimation inter-frame interval time (s)	Star map integration time (s)
> 0.07	0.05	0.05	3.00
< 0.07	0.05	0.25	3.00
< 0.002	0.05	2	3.00

criterion is satisfied, such as the iteration limit. This is detailed in Algorithm 2. In space imaging, sigma-clipping is particularly effective for source finding, where sources are detected as statistically significant intensity peaks. Sigma-clipping is also used to remove pixels or elements with values that are exceedingly high (representing hot pixels, cosmic rays, or other artifacts) or exceedingly low (background noise). In this project, sigma-clipping was used to mask the accumulated pixel regions in the final star map to remove isolated events that likely represent background noise that could otherwise be included in values associated with a genuine source.

---

**Algorithm 2** Sigma clip statistical filtering algorithm

---

```

return Estimated  $x$  and  $y$  direction field velocity
 $V_x, V_y$  at each event segment  $e_{i:j}$  to create event
mosaic
Initialise iterator;
for Value  $V$  in input data  $D$  do
    Calculate mean  $m$  and standard deviation  $\sigma$ ;
    for Value  $V$  in input data  $D$  do
        if  $V \leq m - v\sigma$  or  $V > m + v\sigma$  then
             $V \leftarrow$  masked;
        end if
    end for
    if iterator  $\geq i_{\max}$  then
        continue;
    end if
    iterator++;
end for
```

---

The DBSCAN algorithm is a highly effective unsupervised clustering algorithm. It is commonly used to associate points based on density [32]. DBSCAN is used here to associate events in the motion-compensated star map to detect event sources and noise in the full 3D  $x, y, t$  spatiotemporal event space. It can cluster data with an arbitrary number of clusters, spatial extents, densities, and shapes in the presence of noise [33]. Using DBSCAN, clustering can be performed without priors on the number of sources in the field. This produces clusters that are robust to noisy events and locates faint low-density source clusters. These characteristics are vital for the source finder used in this application given that we do not have a prior on the number of sources within the scene and are likely to encounter noise from the bright central source. Similar statistical clustering algorithms

such as  $K$ -nearest neighbors (KNN) [34],  $K$ -means [35], and mean-shift [36] are not robust to noise, or require a prior on the cluster count. DBSCAN requires only two parameters: the minimum number of points for a cluster to not be considered noise and the minimum association distance  $\epsilon$ . Using DBSCAN, clusters are detected by selecting the central core points, detecting points within an  $\epsilon$  distance, and assigning cluster or noise labels if the number of points is larger than the specified minimum number of points  $P_{\min}$ . The heuristics for selecting the DBSCAN properties are relatively simple [37].  $P_{\min}$  should be set higher than the number of dimensions in the input data to prevent isolated points from being assigned a label. This parameter should be increased further from the default value of 4 when clustering higher-dimensional or highly noisy data [33]. It has also been indicated that a  $P_{\min}$  value two times the number of dimensions is preferable [38]. This value was used in the experiments. However, the  $\epsilon$  distance threshold is more difficult to select and requires knowledge of the data to determine how close points would ideally reside. An expensive adjacency matrix is also required for a high  $\epsilon$ . In this star mapping pipeline, an  $\epsilon$  value of 3 is selected given that source events should have a mutual distance of at least three pixels (which is 4.76 arcsec using the Officina Riccardi-Honders (RH) telescope setup in Astrosite-1).

DBSCAN has been demonstrated to perform effectively in EB vision tasks with event frames [39, 40]. Furthermore, it can process data similar to event streams with an arbitrary number of low-density and high-noise clusters in a high-dimensional spatiotemporal space. However, for practical reasons, DBSCAN cannot be used to cluster events from extended sources. This limitation is owing to the high event rate caused by the brightness and sizeable spatial extent of the extended sources, which results in excessive memory usage owing to the DBSCANs  $O(n^3)$  complexity, largely comprising the adjacency matrix calculation to perform *RangeQuery*. To overcome this limitation, extended event sources with high event rates are used rather than pixel connectivity.

Pixel connectivity is a fundamental conventional computer vision technique for analyzing the relationship between discrete pixels within a neighborhood [41]. The pixel connectivity was measured three times in this pipeline. First, we detected the centroids of the large extended sources as large streaks in the uncompensated

star map for velocity estimation (if present). Second, it was less computationally intensive than DBSCAN to cluster a large volume of events that accompanied extended sources. Finally, as the final step in the source finder, we defined the spatial extent of sources and calculated the spatiotemporal characteristics of event sources, such as the area, extent, and weighted centroid. Source-weighted centroids were used as precise source positions for the astrometric calibration. This pixel connectivity analysis was conducted on a sigma-clipped binary image of either streaks or a motion-compensated star map (depending on where it was used within the pipeline). An eight-connected Moore neighborhood was used here. This implied that events connected as immediate neighbors (including diagonally) belonged to the same neighborhood and originated from the same source.

## 5 Astrometric calibration of event star maps to project EBC measurements to world coordinate frames

In conventional optical astronomy and SSA, data are collected using a frame-based image sensor such as a CCD by exposing the sensor to the sky position of a target and collecting light from the target and surrounding background sources. The exposure time varies based on the task and the brightness of the target. Faint targets require up to 10 s to collect sufficient light, whereas brighter targets may require only 0.5 s. The position of the target in the collected image can be determined in the world frame with a reasonable accuracy using the reported field-center position, known kinematics of the mount, known pixel scale based on the optical configuration, and physical orientation of the sensor in the telescope. The localization accuracy can be improved further by comparing the relative position of the background sources surrounding the target to an established astrophysical survey. This comparison is performed using astrometric calibration [42]. This is an image calibration technique used in astronomy to match a set of observed sources to a star catalogue to determine the world position of the center, angular orientation, and pixel scale of the image. In the case of RSO observations, the specific world coordinate frame can be expressed as a world coordinate system (WCS) or international celestial reference system (ICRS) coordinate frame, with the observer position in a geographic coordinate frame.

The preferable approach for converting event data from pixel coordinates into a world reference frame is similar to that used in conventional space imaging. The high temporal resolution of EBC causes a problem. Events can be reported approximately every 20  $\mu$ s, which is significantly faster than the 500 ms latency of the mount's position reporting. This temporal resolution is typical of most telescope mounts because mount-position-estimates on a timescale shorter than this are generally not required with a relatively long duration of CCD exposures. With the high temporal resolution of the EBC, any high-frequency variation in the mount position owing to wind (where the mount is vulnerable to mounting on a lifting platform), mount mechanical dynamics, or other factors that shift the optics can be detected by the EBC. This motion cannot be accounted for without continuous mount position reporting.

Furthermore, because Astrosite-1 is a mobile observatory with mounts supported by lifting mechanisms, the quality of the pointing models is lower than that of more stable and fixed conventional observatories. This inherent instability further increases the need for accurate calibration to overcome unavoidable pointing offsets. Although the telescope mount provides positions for the geometric field center, these originate from an astrometric calibration calculated using a conventional camera while calibrating the mount. This calculation determines the forward and inverse kinematics of the mount with a reasonable accuracy. However, a rotation is still present owing to the physical rotation of the sensor in the telescope and a translation offset owing to calibration errors and imperfections in the telescope bore sighting.

Because of these practical challenges, astrometric calibration should be used to determine the world projection of events to produce high-precision measurements. Generally performed using “plate solving” in conventional astronomy [43], this practice is vital for converting observation data from the pixel frame into meaningful measurements in a world reference frame.

Astrometric calibration is a well-studied image calibration technique for understanding the transformation between a world coordinate frame and camera coordinate frame. This technique utilizes the extrinsic properties of the camera and the transformation between pixel coordinate frames on the image plane

using the intrinsic parameters of the camera. This is illustrated in Fig. 5. In optical and EB astronomy, image calibration and homography are used to transform frames  $X$  and  $X'$  using a standard homography matrix  $H_{Rt}$  [44]:

$$X' = H_{Rt}X \quad (7)$$

The vector representation of a generic frame transformation using an assumed distortion-free pinhole camera is given by the homography matrix as a homogeneous transformation matrix  $H_{Rt}$  [45]. This transformation projects an image frame  $X_i$  onto the world frame  $X_w$ , which comprises a rotation  $R_{3 \times 3}$  and translation  $d_{3 \times 1}$ .

$$\begin{bmatrix} X_i \\ Y_i \\ Z_i \\ 1 \end{bmatrix} = \begin{bmatrix} R_{xx} & R_{xy} & R_{xz} & d_x \\ R_{yx} & R_{yy} & R_{yz} & d_y \\ R_{zx} & R_{zy} & R_{zz} & d_z \\ f_x & f_y & f_z & \omega \end{bmatrix} \begin{bmatrix} X_w \\ Y_w \\ Z_w \\ 1 \end{bmatrix} \quad (8)$$

In this space-imaging scenario, the optics focus on infinity, and all the sources are projected onto the celestial sphere. Consequently, a simplified approach is used for this scenario to calibrate the two 2D planes. Because the FOV of the EBC is at most 0.4 deg even in relatively wide field RH telescopes, the observable effect of the celestial frame is minimal because the curvature of the frame is essentially zero. In this case, the  $z$ -axis is disregarded [46]. Furthermore, lens distortion is not considered because

astrosite uses reflective telescopes, and no lenses are present in the optical path. The typical calibration transform for this idealized pinhole camera in 2D using “camera matrix”  $P$  is given as

$$\begin{bmatrix} X_i \\ Y_i \end{bmatrix} = P \begin{bmatrix} X_w \\ Y_w \end{bmatrix} \quad (9)$$

where the camera matrix  $P$  describes the intrinsic transformation between the image plane  $X_i$  and camera frame  $X_c$ , and the extrinsic properties of the camera to transform between the camera frame and world frame  $X_w$ , given the focal length components  $f_x, f_y$  and center offset components  $c_x, c_y$ .

$$P = \begin{bmatrix} f_x & 0 & c_x \\ 0 & f_y & c_y \end{bmatrix} \begin{bmatrix} R_{xx} & R_{xy} \\ R_{yx} & R_{yy} \\ d_x & d_y \end{bmatrix} \quad (10)$$

These transformation properties can be estimated by a plate-solving algorithm. The complete  $X_i \rightarrow X_w$  transformation can be expressed in simpler terms as a rotation matrix  $R_{2 \times 2}$ , pixel scaling factor  $\omega$ , and translation of the mount center position  $d_{1 \times 2}$ . Mount center translation is an important factor that describes the offset of the geometric image center in pixel space from the telescope/camera frame origin,  $X_w$ . This transformation is expressed as Eq. (11):

$$\begin{bmatrix} X_w \\ Y_w \end{bmatrix} = \begin{bmatrix} \omega_x \\ \omega_y \end{bmatrix} \left( \begin{bmatrix} R_{xx} & R_{xy} \\ R_{yx} & R_{yy} \end{bmatrix} \begin{bmatrix} X_i \\ Y_i \end{bmatrix} + \begin{bmatrix} d_x \\ d_y \end{bmatrix} \right) + \begin{bmatrix} X_{cw} \\ Y_{cw} \end{bmatrix} \quad (11)$$

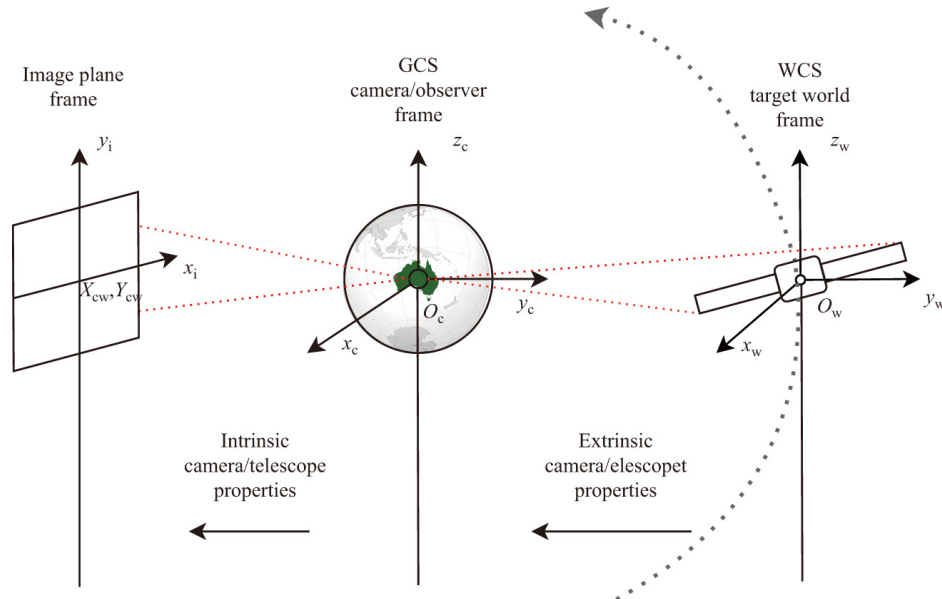


**Fig. 5** Demonstration of the transformation between an RSO in the WCS frame to a GCS camera coordinate frame using the extrinsic properties of the camera/telescope, and the transformation between the pixel coordinate frame on the image plane using the intrinsic parameters of the camera.

If a star map  $H$  can be produced from the event stream, the calibration properties of the field and estimated center can be determined. The calibration properties can then be applied to the pixels of each frame to project all events onto the world coordinate frame as meaningful measurements for SSA tasks. The projected world position of the camera frame origin can be calculated by aligning the image plane frame with the camera coordinate frame through rotation and then, translating the origin of the image plane frame to the camera coordinate frame origin. Finally, the new image plane frame is scaled using the pixel projection scale and translated to the center of the camera's origin in the world frame  $X_{\text{cw}}$  (provided by the plate solver). The pixel scale using the square EBC pixels is identical in both the directions:  $\omega = [\omega_x, \omega_x]^T = [\omega_y, \omega_y]^T$ . Using the solved calibration parameters and a field center from the plate solver  $X_{\text{cw}}$ , the pixels  $[X_i, Y_i] \in [e_{xk}, e_{yk}]$  as events or points on a motion-compensated event star map frame  $H$  can now be projected onto the world frame. This is shown in Fig. 5.

If the star map is excessively large ( $> 10,000$  square pixels before source extraction), motion-compensated star map frames from the entire event stream can be created and calibrated continually. This technique is called multiple point multiple interval (MPMI) calibration. It is the continuous calibration of an event stream using multiple solved star maps as a mosaic. Although computationally intensive, this approach provides low-latency field solutions. This, in turn, enables a variable-speed analysis and improves the position reporting robustness to wind and other short-interval effects that may shift the optics and mount between mount position-reporting intervals. This calibration approach is feasible only with sufficiently detectable background stars to correctly estimate the field velocity for solving the plate. Scenarios in which the FOV has few detectable sources are typically encountered when observing under inferior observation conditions, during high-speed tracking slews, or where long intervals are infeasible. These conditions limit the sensitivity of the EBC and may result in insufficient detected sources to solve the plate. Therefore, an alternative calibration technique is required.

In this case, where a star map cannot be produced or solved, the calibration properties are determined from a previous successful calibration under more favorable conditions, and a previous solution may be used. Any

event within the input event stream can be projected onto a world frame by this calibration solution. However, this transformation requires the reported position of the mount as the assumed projection of the field center in the pixel frame  $X_{\text{ci}}$  in the world frame  $X_{\text{cw}}$ , and the field center estimate  $[\bar{X}_{\text{cw}}, \bar{Y}_{\text{cw}}]^T$  to be valid. In addition, the previously calibrated estimates of  $R$ ,  $d$ , and  $\omega$  could be used in this solution.

Termed in this paper as single point single interval (SPSI) calibration, plate solving may be performed one time per night at a point under favorable conditions with sufficient sources and by an observation technique that maximizes the detection limit (such as a slow tracking slew). Using a sound-pointing model, this blind approach to calibration assumes that the translation offset of the field center and orientation is constant across the sky (except for mount motion effects such as wind, which would require constant target tracking; this is discussed subsequently) [47]. Although SPSI calibration is computationally less expensive than MPMI calibration, this approach relies on using the most current field-center position reported from the mount. Because the temporal resolution of EBC is significantly high, the mount positions should be interpolated such that the event positions in the pixel frame can be transformed to the world frame coordinates at the event time stamp. Interpolation is therefore less accurate and disregards the most high-frequency and unexpected variations in the mount position. Corrections may also be required in the calibration to account for the atmospheric effects and mount motion.

## 5.1 Solving for calibration parameters of an event star map using Astrometrynet

Astrometric calibration was performed using the Astrometrynet plate solver [43]. Astrometrynet is an accurate and widely used package that can be used to plate sky images or tabulate sets of source locations. The Astrometrynet plate was solved in four steps:

- (1) The sub-pixel accurate source positions of stars within the input field was input or calculated by identifying statistically significant peaks in the local image intensity.
- (2) A geometric hash was calculated for the detected subsets of four stars or “quads”.
- (3) A large pre-computed index of known stars was searched for hash codes that matched the quads

to determine a hypothesized alignment between the quad in the query input image and a quad in an index.

- (4) It was verified as a Bayesian decision problem to accurately decide whether the hypothesized alignment was correct and thereby, the hypothesized location, scale, and orientation of the input image on the sky was determined.

Astrometrynet does not require priors. However, information regarding the field can improve the solving time. Astrometric calibration using a local installation of Astrometrynet can be performed within a few seconds when provided with the known pixel scale of the EBC (derived from the optical configuration of the telescope), an approximate pointing center of the star map (obtained from the reported mount position), and a search radius scaled to an approximation of the observation area. Astrometrynet requires a minimum of four sources for calibration if the approximate position and pixel scale are to be provided. The main output is stored in the FIT file containing the calibrated input image and a human-readable header with a summary of the calibration results. These results include the solutions required to perform projections from the pixel frame onto the world frame. These values are the pixel–WCS transformation matrix, pixel scale in the WCS, “CRVAL1/2” RA/DEC center coordinates, “CTYPE1/2” projection type, and “CRPIX1/2” pixel projection and rotation reference points.

## 5.2 GAIA DR2 external and internal source cross-matching

To identify the detected sources in the generated star maps as real-world astrophysical objects, this star mapping pipeline cross-matches the calibrated WCS positions with the GAIA Data Release 2 (DR2) optical astronomy catalogue (the current largest optical survey integrated into Astrometrynet [48]). The Gaia DR2 catalogue contains several source characteristics, namely, source identification and optical magnitude in multiple bands. Additionally, calibration is conducted with the “5200 Heavy” index, which contains sources from the Tycho-2 and Gaia-DR2 catalogue. This index is ideal for fields that are narrower than 1 deg and contain additional Gaia-DR2 information such as the magnitude and catalogue ID.

For each field, the extracted source characteristics are collated and cross-matched. The fields containing exceedingly few sources or those observed during high-speed slews may not contain sufficient sources for a successful calibration. Because all the observations of a given field are conducted with a slew from the same direction and angle, the sources in the unsolved slews can be cross-matched to the solved slews using the common geometric arrangement of each source with respect to the central bright extended source in each observation. The horizontal  $x$  and vertical  $y$  distances between each source and the largest source in the field are calculated for all the fields. These distance measures are then used to associate the sources within the same field. The most likely candidate matches have the closest mutual distance similarity. Inspired by the speed at which sources are matched in Astrometrynet, these matches are located using the nearest-neighbor criteria on a KD-tree. This technique is efficient and scales effectively with 500 total source detections in each field, with  $O(n)$  complexity for storage operations and  $O(\log(n))$ – $O(n)$  for searching operations. Optimized approaches such as these are vital for future SSA systems that are likely to produce significantly more data and have a more significant design focus on low-latency reporting.

Potentially spurious sources detected in unsolved slews can be eliminated if no successful crossmatch is identified (within a five-pixel threshold in the  $x$ - and  $y$ -directions). “Internally”, cross-matching using this method improves the overall robustness of a pipeline by providing every observation for a given field with an astrometric solution when at least one observation is solved. However, spurious detections in the solved fields may not be correlated.

## 6 Overall star mapping, source analysis, and calibration system

The full-star mapping algorithm and calibration pipeline developed in this study are shown in Fig. 6. The pipeline is summarized as follows:

- (1) event star map generation using GNN STT velocity estimation;
- (2) noise filtering using sigma-clipping;
- (3) extended source detection and masking using pixel connectivity;
- (4) point source detection using DBSCAN event clustering;

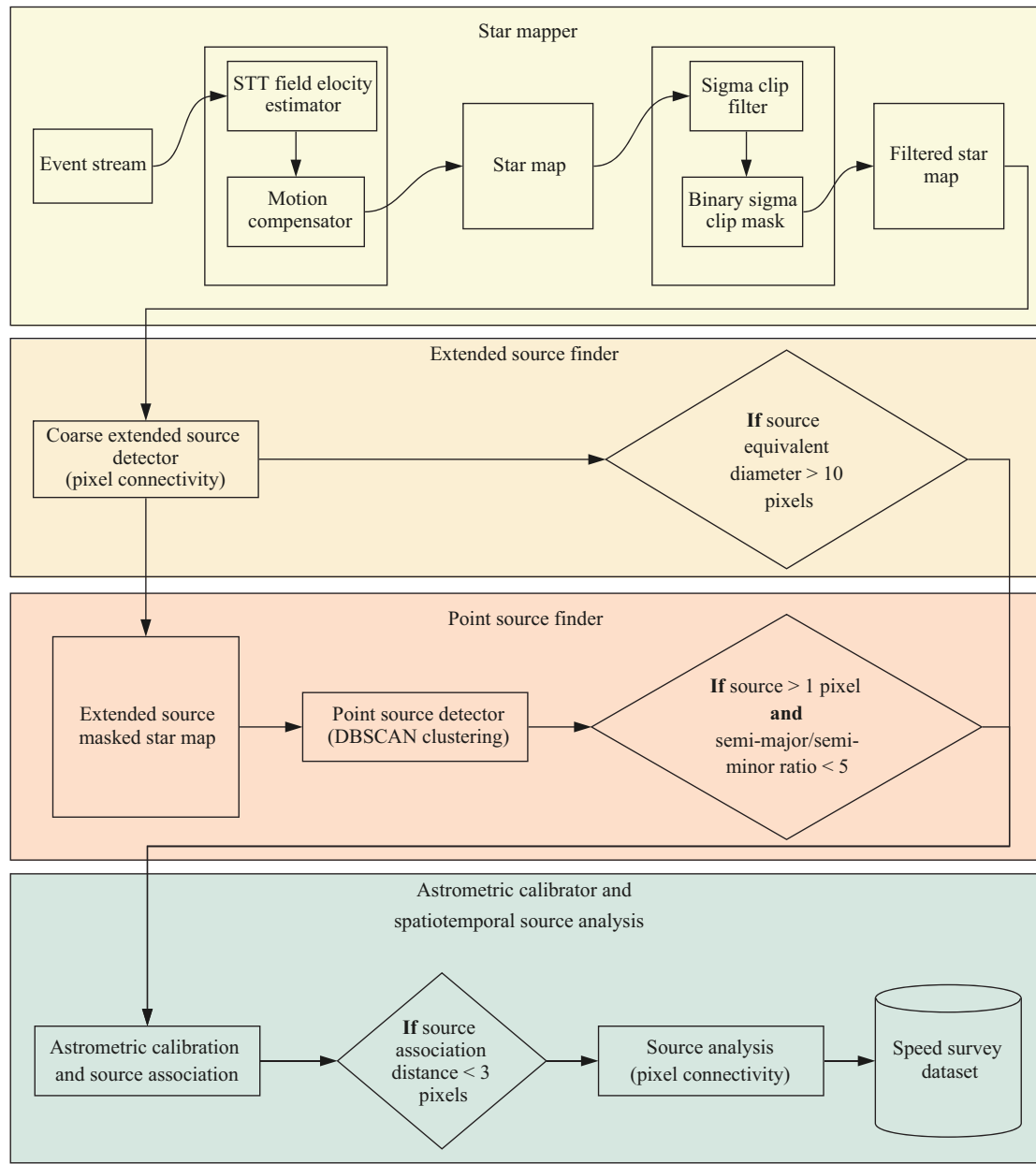


**Fig. 6** Overview of the star mapping, astrometric calibration, and spatiotemporal event source analysis pipeline developed in this study.

- (5) spatiotemporal analysis of detected extended and point sources using pixel connectivity;
- (6) astrometric calibration of the field using an Astrometry.net plate solver of the source positions to project sources in the image frame to the world frame;
- (7) analysis of the relationship between spatiotemporal characteristics of the detected event sources and the photometric characteristics of the underlying astrophysical objects.

## 7 Results

### 7.1 Star mapper performance

The star mapping algorithm developed in this study successfully warped observations collected across four star fields at nine slew speeds to generate star maps containing resolved event sources with sharp spatial features. In Figs. 7–9, the success of the STT velocity-estimation technique is demonstrated by compensating for three field speeds in the Mimosa field. This is the

densest star field with the brightest central source and largest diversity of source brightness. The event streaks accumulated over the integration period are warped onto their trajectories to produce a star field with compact event sources. These star maps contain various sources with diverse magnitudes. Bright extended sources are immediately apparent in the high-speed observations, whereas faint sources gradually become more visible at mid-range and low speeds. In low-speed observations, the sources appear to have fewer wake events and a smaller spatial extent. The source brightness is apparent in these images because brighter targets produce significantly more events and are larger than the faint ones.

The features of the bright extended sources evolved over each observation, and the slew speed gradually resembled an Airy disk. In Fig. 9, the Airy disk is visible around Mimosa in addition to small diffraction spikes. This was anticipated from a nearly diffraction-limited imaging system (therefore, atmospheric effects are still present) and the physical construction of RH Officina in Astrosite-1. In the slow-speed recordings, the on- and off-events form two symmetrical halves of the Airy disk. However, in high-speed recordings, the Airy disk features are more blurred, and off-events produce a long trail of

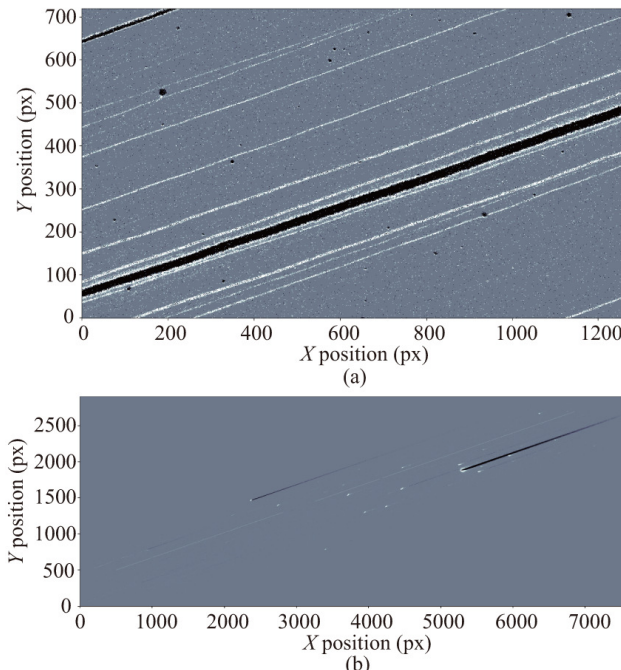


**Fig. 7** Comparison between the original 0.5 s event integration of Field 0 at the highest speed of 0.5 deg/s (a), and the successfully motion-compensated star map (b), where off-events are shown in black and on-events in white.

wake events.

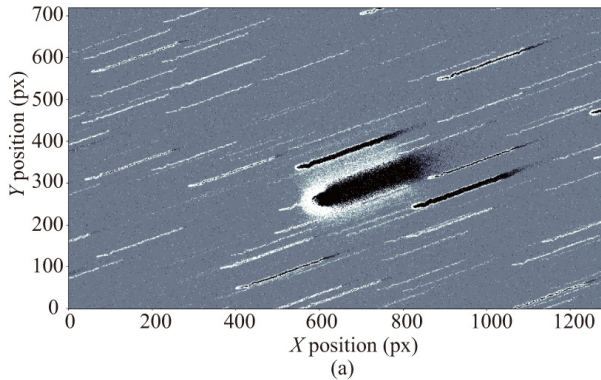
Streaks still present in the warped frames are stationary hot pixels. These are stretched when compensating for mount-slew motion. In the fast-slew accumulated frame in Fig. 7(a), a few off-event point sources are visible. These are the remnant wake events of the sources observed moments before the slew motion through the target field. Certain additional mounting motions are visible in the accumulated event frame in Fig. 8(a). This marginal motion is likely owing to wind. However, it does not appear to have significantly affected the performance of the motion compensation shown in Fig. 9(b).

## 7.2 Source finder and calibration performance

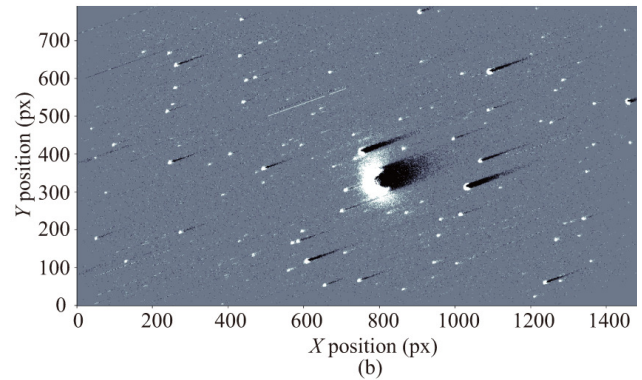
The EB source-finding algorithm proposed and developed in this study successfully detected and localized the sources in star maps across multiple fields and slew speeds. In these star maps, the raw output of the sourcefinder could detect faint point sources. This demonstrated that the proposed system is robust against hot-pixel streaks and isolated noise. In particular, in the high-speed star map (Fig. 10), the wake events produced many false positives. Comparing the star maps generated using only on-events (Fig. 14), fewer noisy regions were detected as sources. However, fewer sources were detected overall. The position accuracy of the source finder was sufficiently high to perform a plate solution in the field to calibrate the motion-compensated star map and associate the detected sources with real-world astrophysical objects.

An astrometric calibration solution was determined for the majority of the fields. As shown in Figs. 10–12, the calibration solution is used to project events as measurements in the pixel frame onto positions in the world frame (J2000). In Fig. 13(a), the error between the astrometric estimate of the pixel scale and the ground truth is small, with an average of 0.0021 arcsec/px. This is an accurate descriptor of the calibration performance. Figure 13(b) illustrates the correlation between high-speed slews and inferior pixel-scale estimates. In these figures, the final filtered and associated output source finder is highly robust to noise, wake events, and hot pixels because only the sources associated with a catalogued source are flagged as genuine event sources.

Figure 15 shows that the number of detectable sources increases as the speed decreases. The figure also shows

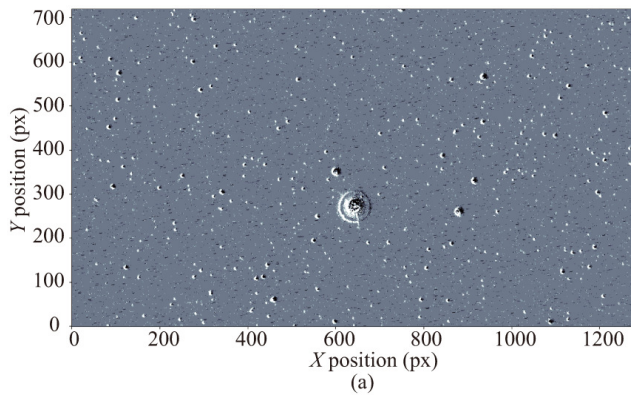


(a)

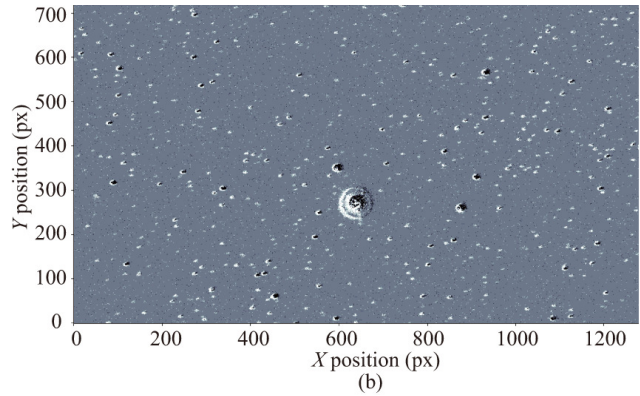


(b)

**Fig. 8** Comparison between the 1.5 s event integration of Field 0 at the mid-range speed of 0.015 deg/s (a), and the correctly motion-compensated star map (b).

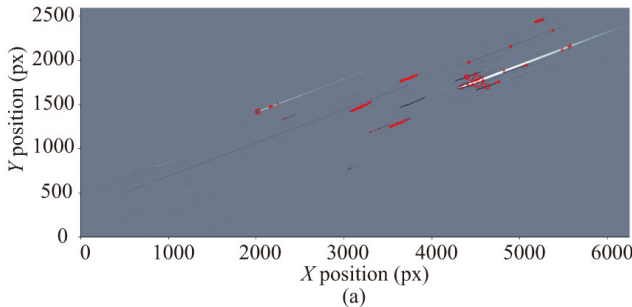


(a)

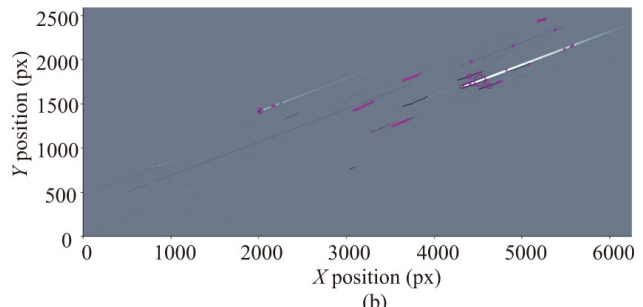


(b)

**Fig. 9** Comparison between the 3 s event integration of Field 0 at the lowest speed of 0.000488 deg/s (a), and the correctly motion-compensated star map (b), where the sharp features of the Mimosa Airy disk are now visible.



(a)



(b)

**Fig. 10** Raw source finder output of the Field 0 high-speed (0.5 deg/s) star map with detected sources circled in red (a), and the filtered source detections (magenta) (b). Here, although the final output is filtered, it is not associated to any astrophysical source because no astrometric solution could be determined for the field. As a result, many erroneous source detections are present in (b) because the calibration solution could not be used for the final source filtering.

the different source counts for each field, with Mimosa Field 0 having the highest number. An abrupt increase in the source count is visible for Field 0 at 0.00075 deg/s. Here, the slew scanned past additional sources that were otherwise outside the FOV for the other scans.

In Fig. 16, the limiting magnitude of the third-generation ATIS EBC from the previously introduced

Ref. [19] (Section 1) is compared with the limiting magnitude of the Gen 4 HD as determined by the star mapper and source finder system developed in this study. These results demonstrate that the limiting magnitude of the Gen 4 HD Astrosite-1 setup is significantly higher at a magnitude of 14.45 during the slowest speed slew, compared with the limit determined using the VGA and

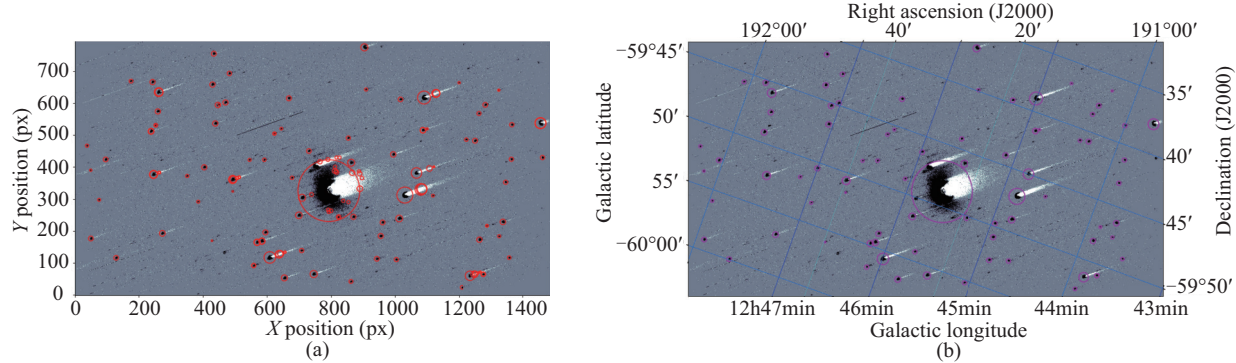


**Fig. 11** Raw source finder output of the Field 0 medium speed ( $0.0015 \text{ deg/s}$ ) star map with detected sources circled in red (a). In (b), an astrometric solution is determined, and the field is projected onto the WCS coordinate frame. The detected sources associated successfully with a catalogued astrophysical source are circled in magenta. Certain sources excessively near Mimosa are filtered erroneously.

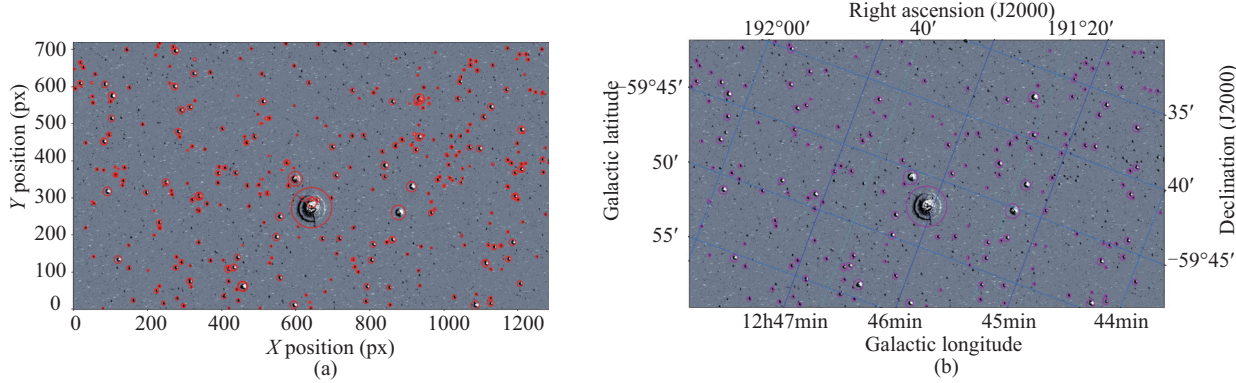


**Fig. 12** Raw source finder output of Field 0 at the lowest speed ( $0.000488 \text{ deg/s}$ ) star map with detected sources circled in red (a). In (b), an astrometric solution is determined, and the field is projected onto the WCS coordinate frame. The detected sources associated successfully with a catalogued astrophysical source are circled in magenta. Field 0 at this speed is shown to contain a large number of detectable sources.

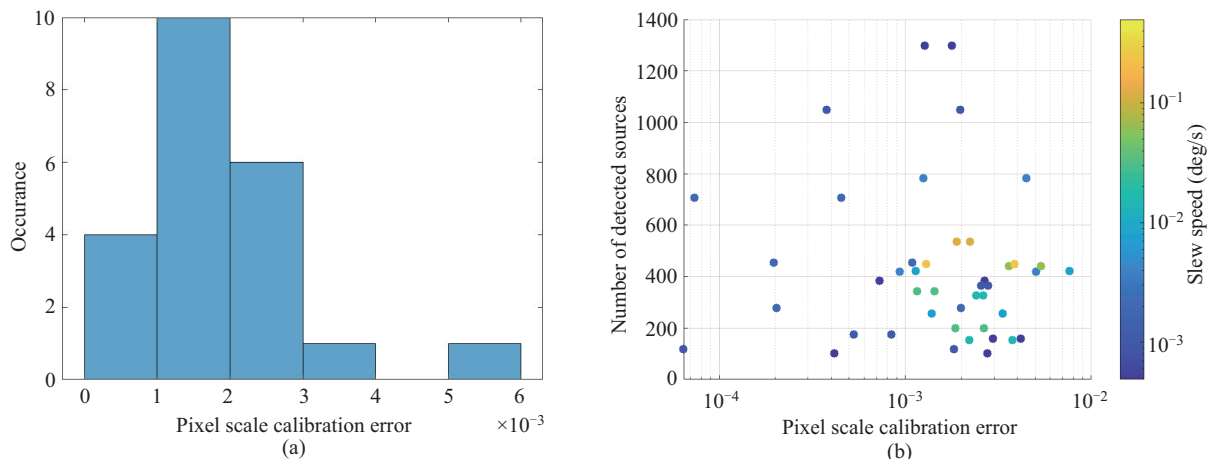


**Fig. 13** In (a), the astrometric calibration error is shown to be consistently small and well within the imposed  $1 \times 10^{-2}$  limit. Number of detected sources vs. pixel calibration error, colored by the slew speed (b), shows that higher slew speeds produce higher pixel scale estimation errors and therefore inferior astrometric solutions, regardless of the source count.

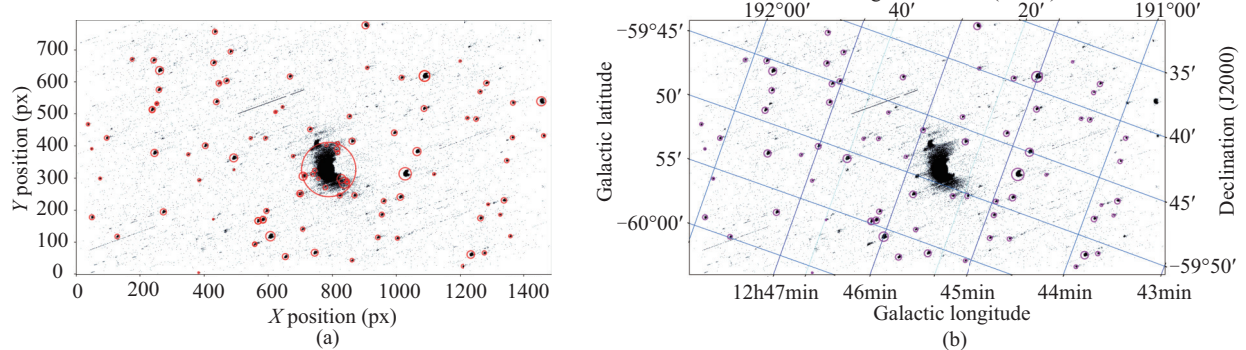


**Fig. 14** Raw source finder output for the Field 0 recording without any off-events in the medium speed star map with detected sources circled in red (a). In (b), an astrometric solution is determined, and the field is projected onto the WCS coordinate frame. The detected sources associated successfully with a catalogued astrophysical source are circled in magenta. The sources in this field are less numerous than in the star field using both on- and off-events. However, fewer spurious false positives are detected in the raw source finder output owing to the significantly fewer wake events.

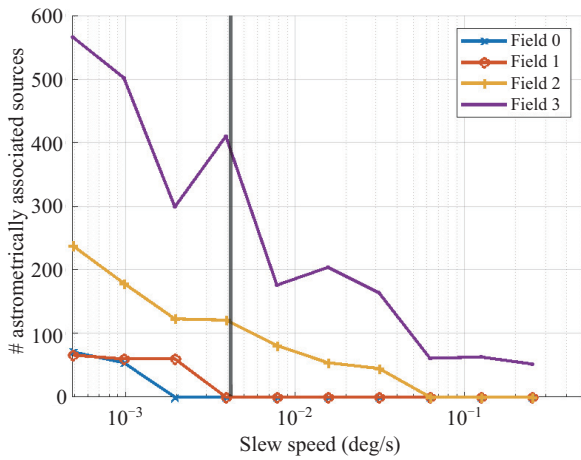


**Fig. 15** Number of detected sources in each field (0–3), where the number of detectable and associated sources increases across the full range of slew speeds from 0.5 deg/s at a sidereal rate of 1200% to 0.000488 deg/s at 11.5%.

HVGA ATIS with an 85 mm f/1.4 (ratio of the focal length and aperture) lens setup of Ref. [19] at a magnitude of 9.6. The lower observed sensitivity (and therefore, higher predicted sensitivity of the Gen 4 HD) is owing to both variations in the characteristics of the EBC and the use of a smaller aperture telescope [19]. This difference in the telescope setup reduced the sensitivity because of the smaller aperture. Sources detected using the Gen 4 HD were also shown to have a higher event rate than those of the previous generation. This indicated that the signal-to-noise ratio (SNR) of the Gen 4 HD is higher, given that the global event rate of EBC is known to be lower [49]. Furthermore, in Fig. 17, the Gen 4 HD is demonstrated to be capable of detecting fainter sources

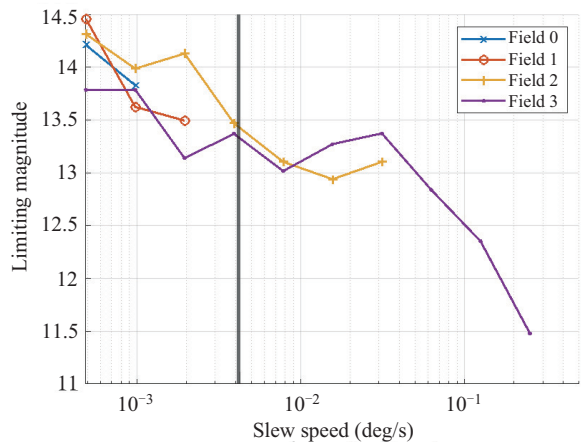


**Fig. 16** Limiting magnitude across a range of speeds using the Gen 4 HD and Astrosite-1 with a lower limiting magnitude (the sidereal rate is shown as a solid black line). Fields without a detection limit occur when no astrometric solution can be determined owing to insufficient detectable sources at such speeds using the EBC.

at higher slew speeds (0.25 deg/s with a sensitivity of up to 11.4) compared with the previous-generation EBC.

Using the output of the source finder and calibrator, the spatiotemporal features and measurement dynamics of the event sources were analyzed at each slew speed. These dynamics were related to the properties of the associated astrophysical sources. The most apparent event source features examined were the spatial extent, event rate, on-/off-event ratio, and centre of mass (COM) offsets.

The event rates of the sources are shown in Figs. 18(a) and 20(a). These increase rapidly with the equivalent diameter, wherein bright sources produce more events by orders of magnitude than smaller faint sources. However,

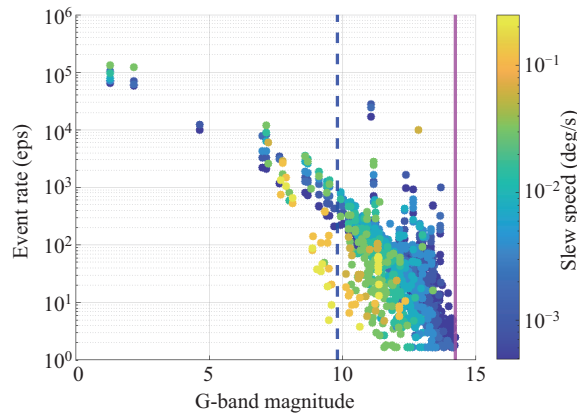
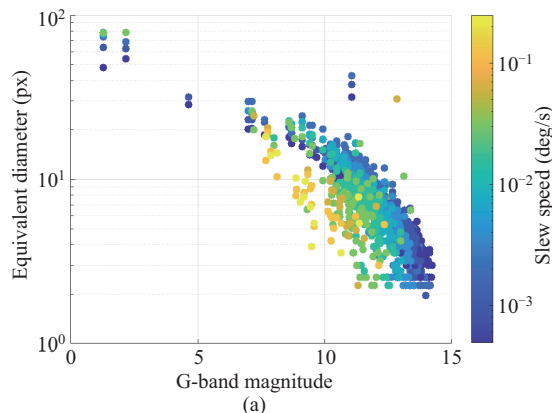


**Fig. 17** Event rate vs. source brightness produced by the pipeline developed in this study using the Gen 4 HD with Astrosite-1. The estimated sensitivity limit of the latest-generation EBC (determined with the proposed system) and the limit of the third-generation EBC reported in Ref. [19] is indicated by the solid magenta line at 14.45 and dashed blue line at 9.6, respectively.

in Fig. 19(b), these bright sources produce fewer off-events than the faint sources regardless of the slew speed. Here, the faint sources observed during high-speed slews produced significantly more off-events than those observed during low-speed slews. Although this trend was influenced by the number of off-events associated with the source by the source finder, at a high speed (where the off-events formed long wake event streaks), these were not associated with the source and were generally filtered out. At lower speeds, this was not the case. Here, sources regardless of size had nearly all the events associated successfully.

As shown in Fig. 18(b), as the source magnitude

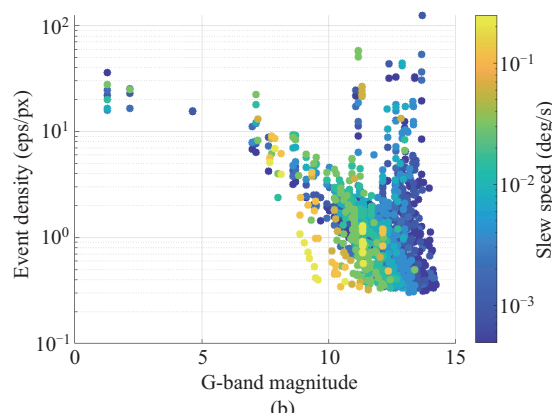


(a)

decreases (brightness increases), the apparent size of the source (estimated using the source equivalent diameter as the minimum diameter of a circle required to enclose the source) increases. Additionally, in Fig. 20(b), the circular extent of sources (1: completely circular; 0: circular) is higher for sources observed during low-speed slews. Here, these appear to be the most circular and symmetrical with comparatively fewer wake events. At higher speeds, the sources begin to spread and elongate along the leading edge.

A consistent offset between the associated source and source finder position is evident in Figs. 21 and 22(a). This constant offset indicates that the source COM is behind the event-leading edge. Although the weighted COM is shown to be behind the true COM, the error between the geometric COM in Fig. 19(b) is shown to be high for all the slews except the slowest ones. The error between the geometric and weighted COM highlights the asymmetrical and unbalanced spatial distribution of the source, particularly without both on- and off-events in the low-speed observations.

On a separate observing night, the speed survey experiments were conducted on Field 0 under windy conditions at an approximate average speed of 20 km/h, as opposed to regular conditions in the remaining dataset of an approximate average of 3 km/h. Notwithstanding the adverse conditions, star mapping and source-finding pipelines were demonstrated to perform robustly under the random motion of the field. Consequently, the wind-affected observations were motion-compensated successfully to produce star maps with diffuse event



(b)

**Fig. 18** (a) Equivalent diameter (smallest bounding circle) and (b) event density vs. the magnitude brightness of sources, colored by the slew speed (deg/s). The magnitude limit decreases with the slew speed until an evidently lower magnitude limit of 14.45 is visible at the lowest speed. The source spatial extent and density are shown to increase with the source brightness.

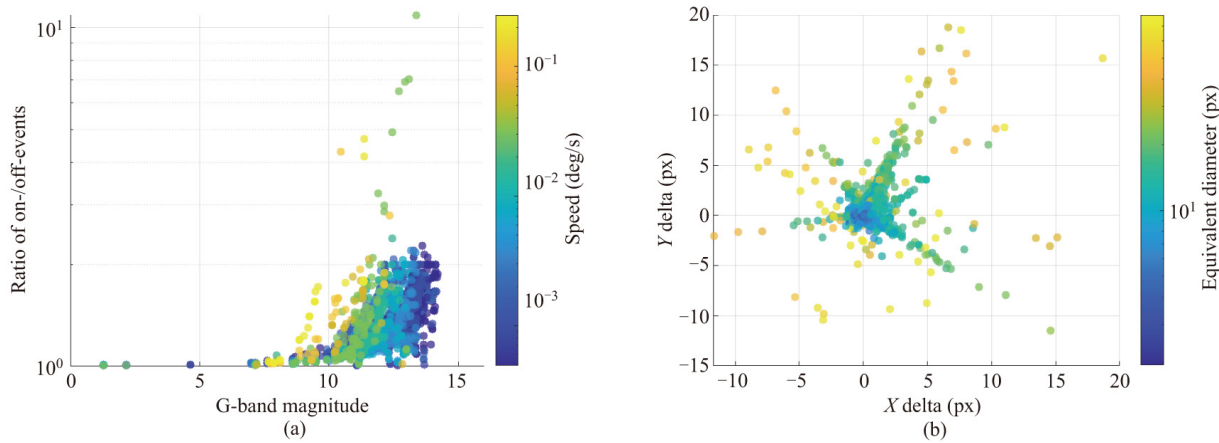


**Fig. 19** (a) On-/off-event ratio vs. brightness magnitude, colored by slew speed, which shows that the faint sources detected at mid-range speeds produce the most off-events. The off-event count is shown not to exceed the on-event count. In (b), the error between the geometric COM and weighted COM is shown to grow rapidly with the apparent source size.

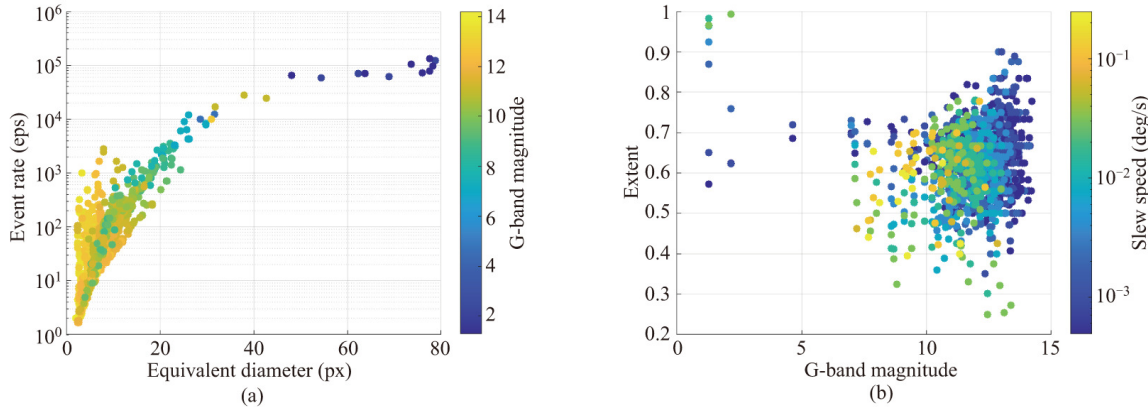


**Fig. 20** (a) Event rate vs. equivalent diameter colored by magnitude brightness, showing that the event rate of a source increases rapidly with the apparent source size, which is a function of the source brightness. (b) Extent vs. magnitude brightness colored by slew speed, where the extent (1: most circular) shows that the brightest sources are the most circular.

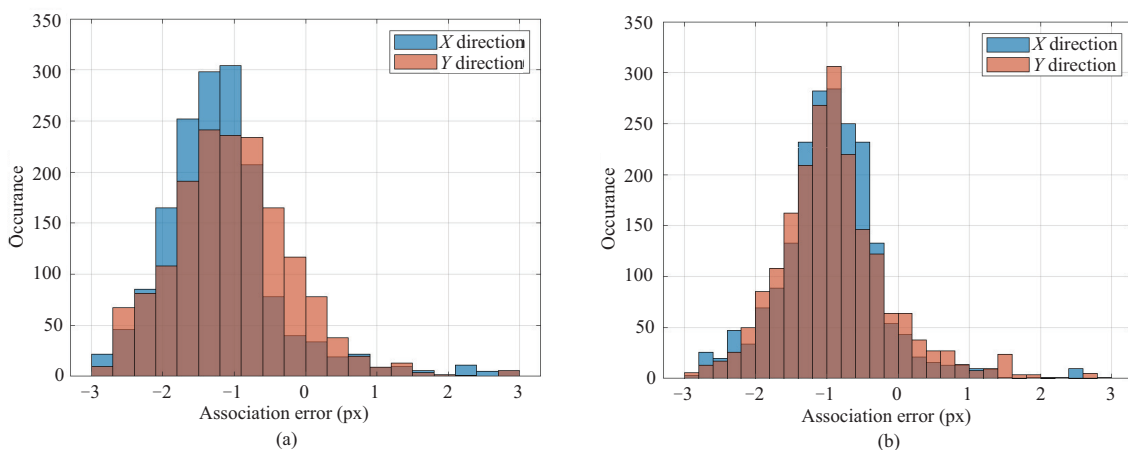


**Fig. 21** Directional association error distribution in the  $x$ - and  $y$ -directions for (a) mono polarity (only on events) star maps and (b) dual polarity star maps, which shows that source COM has a consistent position offset behind the actual source COM. This effect is less pronounced in mono-polarity star maps.

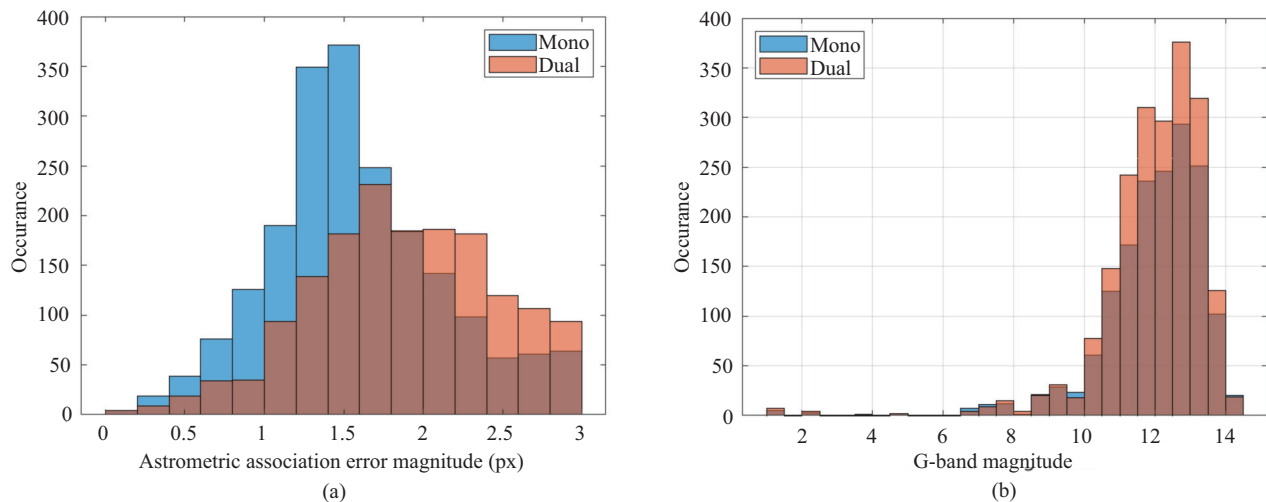


**Fig. 22** Distribution of the astrometric association error between source positions on the calibrated star map and the closest catalogued astrophysical source. Using only on-events in the star map (mono), a lower association error is observed compared with the use of both on- and off-events (dual) (a). In (b), the distribution of source brightness detected for mono and dual polarity star maps indicate that the overall number of detectable sources is lower for mono star maps regardless of the magnitude.

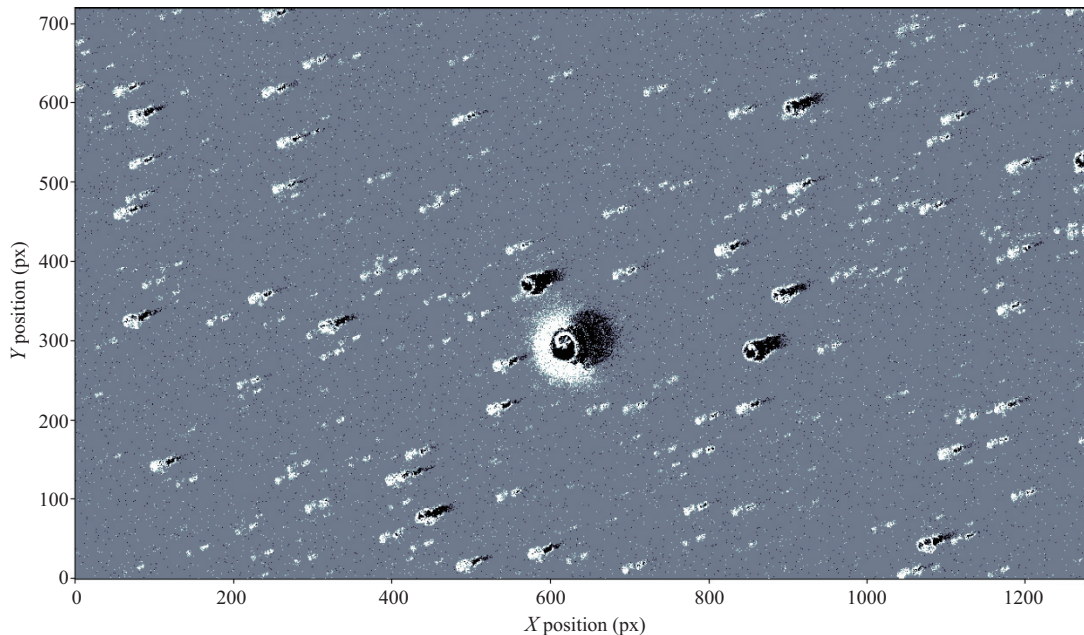


**Fig. 23** Raw source finder output of Field 0 observed in windy conditions where the adverse effects are most apparent at a slew speed of 0.002 deg/s. Event sources in the star map are highly diffuse and resolved inadequately.

sources, as shown in Fig. 23. The source finder also successfully detected these resulting event sources, as shown in Fig. 24(a). These were then used to calibrate the field in Fig. 24(b). Although the wind observations were processed successfully, these contained significantly fewer detectable sources across all the magnitudes as shown in Fig. 25(a). Moreover, fewer associated

sources were detected, as demonstrated by the reduced source detections between the raw source finder output and calibrated output. Here, the inferior source COM estimates failed to produce sufficient source associations. In addition to the reduced sensitivity and inferior COM estimates, the spatiotemporal characteristics of the event sources observed under windy conditions differed from

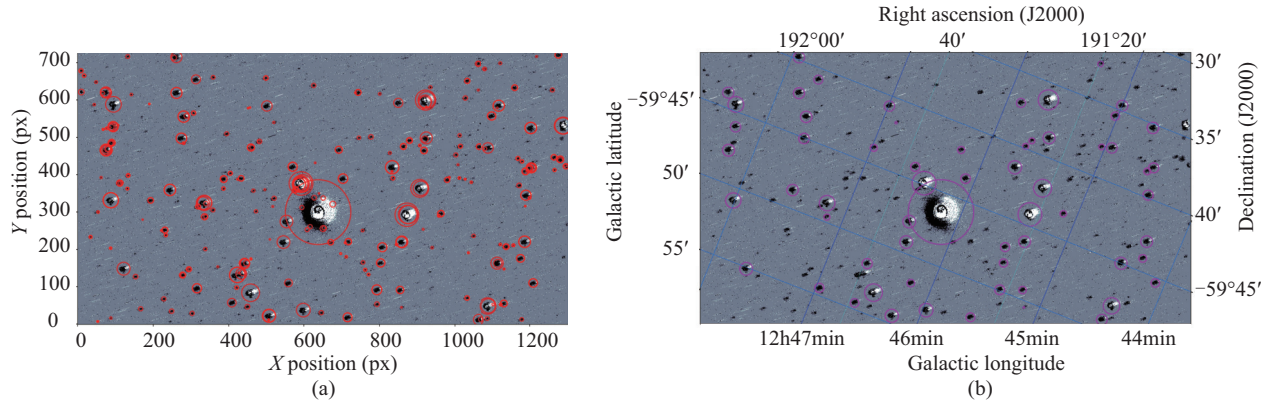


**Fig. 24** Raw source finder output of Field 0 observed in windy conditions where the adverse effects are most apparent with a slew speed of 0.002 deg/s. (a) A star map with detected sources circled in red. In (b), an astrometric solution is determined, and the field is projected onto the WCS coordinate frame. The detected sources associated successfully with a catalogued astrophysical source are circled in magenta. Field 0 at this speed is shown to contain a large number of detectable sources.

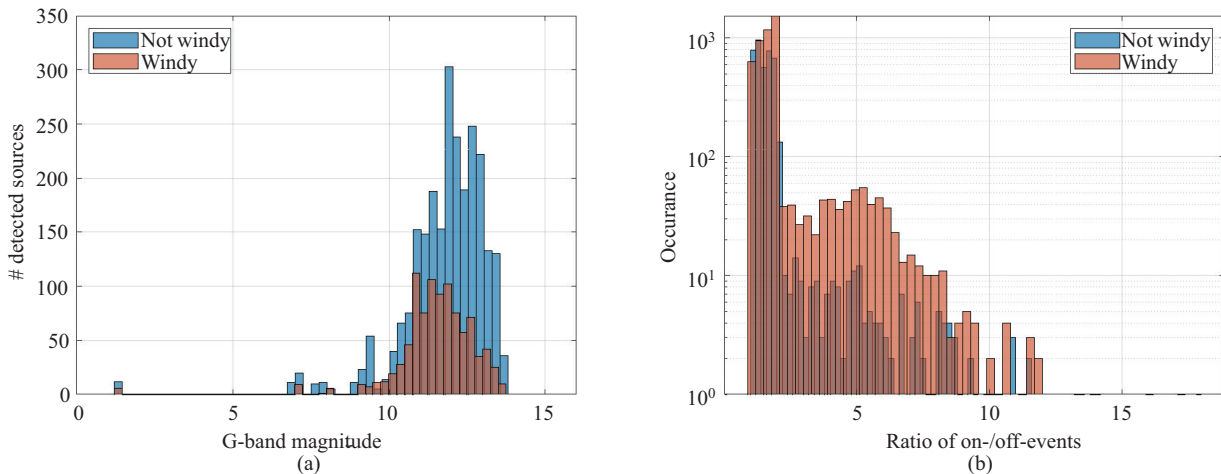


**Fig. 25** (a) Comparison of the distribution between the brightness of detected sources for windy and non-windy observations shows that windy conditions reduce the number of detectable sources. In (b), the on-/off-event ratio for windy recordings shows that sources detected in windy conditions produce significantly more off-events.

those observed without wind. The event sources observed under these conditions produced higher event rates, event densities, and equivalent diameters. This is illustrated in Figs. 25(b) and 26(a). These characteristics are consistent with targets undergoing additional mutual motion. This causes the incoming source light to move randomly in the field, thereby increasing the detectable contrast and spatial extent of the PSF. Additionally, in Fig. 25(b), the sources observed under wind conditions produced significantly more off-events.

## 8 Discussion

In these experiments, the performance of the proposed pipeline was demonstrated successfully. Furthermore,

the varying spatiotemporal characteristics of the event sources were analyzed at varying slew speeds. This system provides an accurate and effective solution for source-finding and astrometric calibration. This is the first solution in the literature that uses only real-world collected EB data for source finding and astrometric calibration. In addition to its use as an analysis tool, the potential role of the pipeline developed in this study within a full-fledged SSA system is to perform an accurate offline conversion of the RSO state estimates in the image plane to a world coordinate frame.

Overall, the proposed star mapper and source finder operated successfully and produced a low astrometric calibration offset. Using the specified optical setup, the

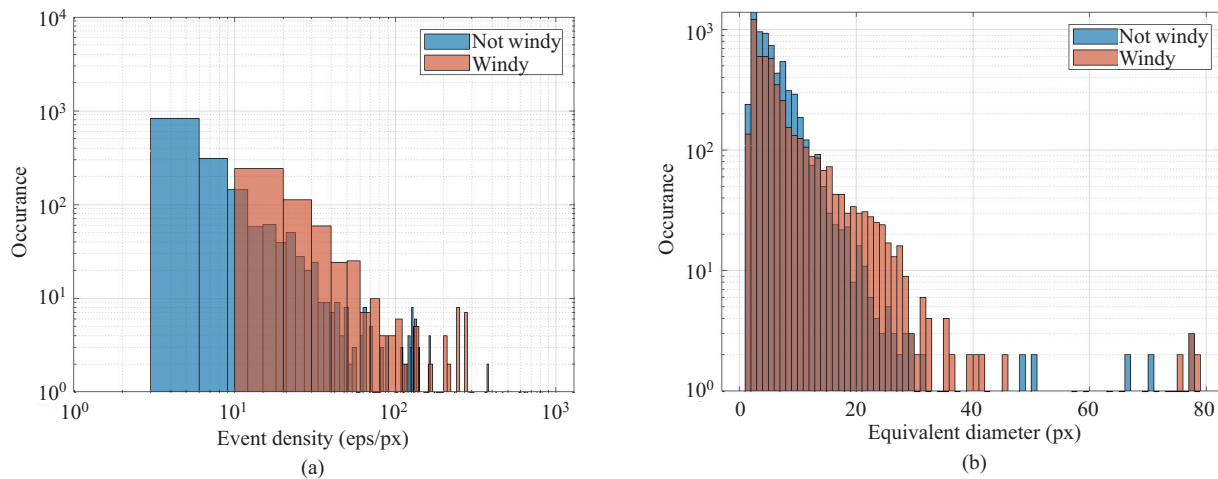


**Fig. 26** (a) Comparisons between the distribution of event density and (b) equivalent diameter for windy and not-windy observations. Here, the event density and spatial extent of sources are shown to be higher for sources detected in windy conditions.

limiting magnitude of the Gen 4 HD was determined to be 14.45. This is largely based on the capabilities of the algorithms used in this study and would improve in future work with several enhancements as the overall space imaging system develops. The sources increased in apparent size and event rate as the brightness increased (magnitude decreased). Faint-point sources produced more off-events than bright sources. Wake events produced by off-events were the most prominent at high speeds and were difficult to process. Notwithstanding the challenges involved in processing off-events, their use improves the source finder performance in terms of source count and COM estimation accuracy. Although this pipeline operates robustly under wind conditions, these conditions reduce the number of detectable sources and sensitivity limit while increasing the event density, apparent spatial extent, and number of off-events. The difference between the geometric center of the sources and the weighted center is non-negligible. Moreover, a consistent offset is detectable owing to the wake events. A significant offset exists between the geometric COM and weighted COM of the sources. This increases with the apparent spatial extent. A consistent offset is observed between the source-weighted COM and the COM of the associated underlying astrophysical source. Here, the event source COM appears to proceed with the catalogued source by approximately 1.5 pixels.

According to these results, the number of detectable sources increased as the slew speed decreased. However,

an upper bound on the tradeoff between the sensitivity limit and slew speed was not observed. Additional low-speed scanning slews are required in future studies to determine the point at which the slew speed becomes exceptionally low. At this point, the event sources produce an excessively marginal contrast, thereby resulting in inferior sensitivity. The low-level hardware control of the mount and telescope mount support should be improved to ensure that the telescope is sufficiently stable to produce low-speed mount slews with precise motion only in the intended direction of travel. Although the mount was instructed to move at a constant speed during the data collection, additional uncompensated motions could introduce mutual motion and vibration. Future studies would discard the assumption that a constant field velocity would occur throughout the observation period. Rather, an multiple target tracking (MTT) algorithm (as opposed to the STT approach used in this study) would be employed with a shorter time interval to adequately compensate for any other mutual motion.

In these experiments, the off-events produced numerous spurious events and artifacts. This phenomenon caused the astrometric association error between the sources and catalogued astrophysical objects to be higher in star maps with only one event. However, including both the event polarities improved the symmetry of event sources in low-speed observations, reduced the source measurement complexity, and facilitated tracking. Furthermore, for

both the polarities, the total source count across the brightness range increased because the event sources had an overall higher event rate. This increase can be considered as an increase in the SNR. However, further investigation is required to precisely classify events as signals or noise.

The high temporal resolution of the EBC is exemplified by its robust performance in the presence of wind. Although the pipeline performed well under adverse wind conditions, a reduction in the number of detectable sources was observed owing to several factors. Primarily, the wind conditions caused the optics to move, thereby spreading the oncoming light over a larger region on the image plane. This movement adversely affected the COM estimation accuracy and detection limit of the EBC. This adverse effect is similar to the problems observed during observations using narrow FOV telescope imaging systems, where the sensitivity can be reduced as the contrast spreads across an excessive number of pixels [11]. However, the reduced source count was also a consequence of the star mapper failing to correctly compensate for varying field motions to generate compact sources. A comparison between the fields observed during cloudy conditions indicates that a mutual motion between the EBC and mount is required to overcome the perfect tracking problem and generate sufficient contrast to detect the sources. However, these experiments showed that if this motion is random and exceedingly large, the sensitivity limit increases, and the sources become more difficult to detect as these become more diffuse. A more accurate quantification of the vibration induced by wind in the mount would be included in future work using an inertial measurement unit (IMU) mounted on the telescope.

The high dynamic range of the EBC was apparent while observing fields containing both bright and faint sources, which would typically not be visible in a conventional CCD and may saturate under similar conditions. Using the specified optical setup, the limiting magnitude of the Gen 4 HD was determined to be 14.45. This limitation was largely based on the capabilities of the algorithms used in this study. Furthermore, this limitation can be improved with alternate optics or improved star mapping, source-finding, and calibration algorithms. This would be the focus of future studies. Compared with the results in Ref. [19], the Gen 4 HD improved dramatically from the previous generation EBCs (which was observed to have

a limiting magnitude of 9.6). The improved performance of the newer-generation sensor was largely owing to the increased pixel resolution and backside illuminated pixel design for a larger fill factor and lower photon noise. As discussed, the limiting magnitudes of the previous generation of EBC were affected by the author's use of a smaller aperture. In the slow-speed slew experiments, the Airy disk of bright sources was visible using the Gen 4 HD because of the increased sensitivity compared with the previous generation of sensors. Because space imaging studies using Gen 4 HD have not been published, this is the first known observation of an Airy disk pattern surrounding bright astrophysical sources using EBC.

Although this system is accurate, performs as intended, and contains well-optimized components, it does not perform in real time. In this case, calibration is only a postprocessing step for converting pixel space measurements to WCS. Therefore, it does not need to run in real time, online, or in parallel with an EB RSO tracker such as fast iterative extraction of salient targets for tracking asynchronously (Fiesta) [28]. Rather, it can run offline after observations to produce accurate measurement sets for input into a relevant mission system. The pixel positions and coarse angular measurements are sufficient for all the other tasks such as closed-loop tracking. Within the filtering and clustering stages of this pipeline, several parameters exist (such as the  $\epsilon$  distance in DBSCAN). These can consume excess memory if the dense event regions are split into smaller regions that can be detected as individual sources. For example, DBSCAN, with an excessive number of input clusters and a large  $\epsilon$  ( $\geq 2$ ), requires a large adjacency matrix to be calculated and stored at runtime. This can be memory intensive.

The proposed system does not currently account for atmospheric effects. An inferior atmospheric observation is likely to produce variations in event source measurement statistics and reduce the accuracy of source position estimates. This may result in an inferior astrometric fit and a similarly reduced pixel-to-world transform accuracy. The variations in the photometric characteristics of the observed sources caused by the atmosphere effects mainly affect the limiting sensitivity. This is because we do not currently provide the Astrometrynet with photometric information. Future work would focus on quantifying these astrometric effects to better understand how the collected data are affected.

If similar observations are collected from an EB system in orbit, the same motion compensation techniques can be used to generate an event mosaic capable of being plate solved to calculate the pixel-to-world transformation. However, without atmospheric effects, we would rely on the mutual motion of the on-orbit system to generate contrast in EBC. Additionally, in future work we would assess the capabilities of more complex MTT Bayesian trackers in difficult scenarios without a constant or linear field motion.

The significant difference between the source-weighted COM and geometric COM reinforces the difficulty of the EB SSA tracking tasks. Consequently, simple shape/kernel-based or feature template-tracking approaches that are common in the EB vision literature are likely to be incapable of accurately estimating the COM of a source. The apparent offset between the astrophysical source and weighted COM implies that the COM state may not be estimated by only the position of events because events appear along the leading edge of the target and are not ensured to represent the source COM. These results show that the majority of events occur on the leading edge. That is, the weighed COM proceeds the true source COM by a significant offset of approximately 1.5 pixels (or 2.4 arcsecond). This consistent offset further intensifies the need for extended target tracking (ETT), which assumes that a target has a non-negligible spatial extent as opposed to the more conventional point target tracking. In addition, because the COM error increases for larger extended sources compared with point sources, an ETT tracking system should preferably be developed. Such a tracker would be capable of dynamically estimating the COM offset and true target COM based on the target extent. However, ETT algorithms are complex and challenging to implement.

These experiments demonstrated the differences in measurement properties between compact faint point sources and bright extended sources. Bright sources appear with a significantly larger spatial extent and

higher event rate, thereby producing fewer off-events than fainter point sources. The difference in the event rate and size of bright sources indicates that a method to filter or mask bright objects may be required to prevent saturation or dramatic variations in processing times when these are within the FOV. Techniques to better estimate the COM of these sources should be developed, particularly when EBC is to be used in large-aperture narrow FOV imaging systems (where their apparent size could be significantly larger and even faint sources would appear to a large extent). In this study, the effect of the EBC bias settings was not analyzed. These biases control the overall behavior of the EBC such as the on-/off-event threshold. Future studies would focus on dynamically tuning these biases in response to scene dynamics or SSA tasks.

The relationships determined between the event rate and equivalent diameter of event sources can be used to estimate target brightness variations in short time-intervals, which is highly challenging with current conventional sensors. Estimating these photometric properties at a high speed is advantageous because such a technique can capture valuable information for the difficult task of RSO characterization. In Table 5, the track capacity (the number of targets observable/trackable within a given period of time, generally one “night”) is contextualized at the limits of the slew speed range examined in this study. GEO belt scanning is a common SSA task where all GEOS are observed sequentially along the orbit and un-cued or lost GEOS can be identified. These slew speed ranges indicate that a scanning observation could be performed using a 100 h scan with an emphasis on the sensitivity at 0.000488 deg/s, or a rapid scan with an emphasis on speed can be performed in 6 min at 0.25 deg/s. A similar set of observations with the same trade-off can be performed for a region scan with a 1 deg<sup>2</sup> area in an arbitrary sky region within 59 min and 3.55 s, respectively. Within these scanning speeds, an EB space imaging system can be used for rapidly surveilling bright targets for the entire

**Table 5** Contextualizing the high capacity observing capabilities of the 4th Gen HD, where the pixel scale is 1.584 arcsecond per pixel and the GEO belt is 180 deg × 0.5632

Slew speed	Limiting magnitude	Time to scan 1 deg <sup>2</sup>	Time to scan GEO belt
0.0005 deg/s (1.8 arcsec/s)	14.45	59 min	100 h
0.5 deg/s (1800 arcsec/s)	11.4	3.55 s	6 min

FOR (the entire observable sky of the system as opposed to the FOV, which is the instantaneous coverage of the sensor). Overall, the wide operating range and potential for rapid characterization are unique capabilities in space imaging. These further motivate the use of EBC in SSA.

Although the literature and this study focused on developing software solutions for calibration, the preferable solution may lie in the specific EB space imaging hardware for EB imaging. In addition to the challenges of calibrating an EB or generating a pointing model using EB data (an inverse kinematic model between the sky coordinates and joint motion in the mount), the central problem is the unsynchronized and uncoordinated clocks and the difference in temporal resolution between the telescope mount position (given by the encoder read-out) and EBC.

## 9 Conclusions

This study developed a star mapping and source-finding algorithm to generate resolved images of event sources at varying speeds to calibrate the Gen 4 HD EBC for accurate measurement acquisition for real-world space imaging tasks. This star mapping and calibration pipeline is the first automatic and fully EB system in the literature. It has been constructed and tested using real-world EBC observations and without scene information from conventional imaging sensors. By calibrating the sources detected using the EBC, a solution for the difficult problem of converting raw event measurements into real-world measurements in a world coordinate frame was developed. In the speed survey experiments, the spatiotemporal characteristics of the detected event sources were related successfully to the photometric characteristics of the detected astrophysical objects. The results of this pipeline established a foundation for principled space imaging and SSA techniques using EBC, with an improved understanding of the spatiotemporal features and measurement dynamics of event sources. In future work, several enhancements including improved star mapping, calibration, and source-finding algorithms are likely to further extend the sensitivity limits and capabilities of Gen 4 HD for space imaging and SSA.

## Author contributions

NOR conducted the investigation, developed the methodology and software, performed the validation,

and wrote the original draft. AM collected the data used in this study and reviewed the final manuscript. SA, NT, GC, and AvS reviewed and edited the original draft, supervised the project, and contributed to the methodology.

## Funding note

Open Access funding enabled and organized by CAUL and its Member Institutions.

## Declaration of competing interest

The authors have no competing interests to declare that are relevant to the content of this article.

## References

- [1] Liou, J. C., Johnson, N. L. Risks in space from orbiting debris. *Science*, **2006**, 311(5759): 340–341.
- [2] Bobrinsky, N., Del Monte, L. The space situational awareness program of the European Space Agency. *Cosmic Research*, **2010**, 48(5): 392–398.
- [3] Cohen, G., Afshar, S., Morreale, B., Bessell, T., Wabnitz, A., Rutten, M., van Schaik, A. Event-based sensing for space situational awareness. *The Journal of the Astronautical Sciences*, **2019**, 66(2): 125–141.
- [4] Mahowald, M. The silicon retina. In: *An Analog VLSI System for Stereoscopic Vision*. Boston, MA, USA: Springer, **1994**: 4–65.
- [5] Mead, C. How we created neuromorphic engineering. *Nature Electronics*, **2020**, 3(7): 434–435.
- [6] Gehrig, D., Rebecq, H., Gallego, G., Scaramuzza, D. Asynchronous, photometric feature tracking using events and frames. In: Proceedings of the European Conference on Computer Vision, **2018**: 750–765.
- [7] Gallego, G., Delbruck, T., Orchard, G., Bartolozzi, C., Taba, B., Censi, A., Leutenegger, S., Davison, A., Conradt, J., Daniilidis, K., et al. Event-based vision: A survey. *IEEE Transactions on Pattern Analysis and Machine Intelligence*, **2019**, 44(1): 154–180.
- [8] Chen, G., Cao, H., Conradt, J., Tang, H. J., Rohrbein, F., Knoll, A. Event-based neuromorphic vision for autonomous driving: A paradigm shift for bio-inspired visual sensing and perception. *IEEE Signal Processing Magazine*, **2020**, 37(4): 34–49.
- [9] Cheung, B., Rutten, M., Davey, S., Cohen, G. Probabilistic multi hypothesis tracker for an event based sensor. In: Proceedings of the 2018 21st International Conference on Information Fusion, Cambridge, UK, **2018**: 933–940.
- [10] Afshar, S., Nicholson, A. P., van Schaik, A., Cohen, G. Event-based object detection and tracking for space

- situational awareness. *IEEE Sensors Journal*, **2020**, 20(24): 15117–15132.
- [11] Ralph, N., Maybour, D., Bethi, Y., Cohen, G. Observations and design of a new neuromorphic event-based all-sky and fixed region imaging system. In: Proceedings of the Advanced Maui Optical and Space Surveillance Technologies Conference, Maui, Hawaii, USA, **2019**: 71.
- [12] Cohen, G., Afshar, S., van Schaik, A. Approaches for astrometry using event-based sensors. In: Proceedings of the Advanced Maui Optical and Space Surveillance Technologies Conference, Maui, Hawaii, USA, **2018**: 25.
- [13] Chin, T. J., Bagchi, S., Eriksson, A., van Schaik, A. Star tracking using an event camera. In: Proceedings of the 2019 IEEE/CVF Conference on Computer Vision and Pattern Recognition Workshops, Long Beach, CA, USA, **2019**: 1646–1655.
- [14] Bagchi, S., Chin, T. J. Event-based star tracking via multiresolution progressive Hough transforms. In: Proceedings of the 2020 IEEE Winter Conference on Applications of Computer Vision, Snowmass, CO, USA, **2020**: 2132–2141.
- [15] Sikorski, O., Izzo, D., Meoni, G. Event-based spacecraft landing using time-to-contact. In: Proceedings of the 2021 IEEE/CVF Conference on Computer Vision and Pattern Recognition Workshops, Nashville, TN, USA, **2021**: 1941–1950.
- [16] Jolley, A., Cohen, G., Joubert, D., Lambert, A. Evaluation of event-based sensors for satellite material characterization. *Journal of Spacecraft and Rockets*, **2022**, 59(2): 627–636.
- [17] Roffe, S., Akolkar, H., George, A. D., Linares-Barranco, B., Benosman, R. B. Neutron-induced, single-event effects on neuromorphic event-based vision sensor: A first step and tools to space applications. *IEEE Access*, **2021**, 9: 85748–85763.
- [18] Żołnowski, M., Reszelewski, R., Moeys, D. P., Delbrück, T., Kamiński, K. Observational evaluation of event cameras performance in optical space surveillance. In: Proceedings of the NEO and Debris Detection Conference, Darmstadt, Germany, **2019**.
- [19] McMahon-Crabtree, P. N., Monet, D. G. Commercial-off-the-shelf event-based cameras for space surveillance applications. *Applied Optics*, **2021**, 60(25): G144–G153.
- [20] Oliver, R., Savransky, D. Event-based sensor model for space domain awareness. In: Proceedings of the Advanced Maui Optical and Space Surveillance Technologies Conference, Maui, Hawaii, USA, **2021**.
- [21] Joubert, D., Marcireau, A., Ralph, N., Jolley, A., van Schaik, A., Cohen, G. Event camera simulator improvements via characterized parameters. *Frontiers in Neuroscience*, **2021**, 15: 702765.
- [22] Gallego, G., Rebecq, H., Scaramuzza, D. A unifying contrast maximization framework for event cameras, with applications to motion, depth, and optical flow estimation. In: Proceedings of the 2018 IEEE/CVF Conference on Computer Vision and Pattern Recognition, Salt Lake City, UT, USA, **2018**: 3867–3876.
- [23] Stoffregen, T., Kleeman, L. Event cameras, contrast maximization and reward functions: An analysis. In: Proceedings of the 2019 IEEE/CVF Conference on Computer Vision and Pattern Recognition, Long Beach, CA, USA, **2019**: 12292–12300.
- [24] Gallego, G., Gehrig, M., Scaramuzza, D. Focus is all you need: Loss functions for event-based vision. In: Proceedings of the 2019 IEEE/CVF Conference on Computer Vision and Pattern Recognition, Long Beach, CA, USA, **2019**: 12272–12281.
- [25] Liu, D. Q., Parra, Á., Chin, T. J. Globally optimal contrast maximisation for event-based motion estimation. In: Proceedings of the 2020 IEEE/CVF Conference on Computer Vision and Pattern Recognition, Seattle, WA, USA, **2020**: 6348–6357.
- [26] Wang, Y. F., Yang, J. Q., Peng, X., Wu, P., Gao, L., Huang, K., Chen, J. B., Kneip, L. Visual odometry with an event camera using continuous ray warping and volumetric contrast maximization. *Sensors*, **2021**, 22(15): 5687.
- [27] Zhu, A. Z., Yuan, L. Z., Chaney, K., Daniilidis, K. Unsupervised event-based learning of optical flow, depth, and egomotion. In: Proceedings of the 2019 IEEE/CVF Conference on Computer Vision and Pattern Recognition, Long Beach, CA, USA, **2019**: 989–997.
- [28] Ralph, N., Joubert, D., Jolley, A., Afshar, S., Tohill, N., van Schaik, A., Cohen, G. Real-time event-based unsupervised feature consolidation and tracking for space situational awareness. *Frontiers in Neuroscience*, **2022**, 16: 821157.
- [29] Foster, B. J., Ye, D. H., Bouman, C. A. Multi-target tracking with an event-based vision sensor and a partial-update GM-PHD filter. *Electronic Imaging*, **2019**, 31(13): 127-1–127-7.
- [30] Bertin, E., Arnouts, S. SExtractor: Software for source extraction. *Astronomy and Astrophysics Supplement Series*, **1996**, 117(2): 393–404.
- [31] Kleyna, J. T., Wilkinson, M. I., Evans, N. W., Gilmore, G. A photometrically and kinematically distinct core in the Sextans dwarf spheroidal galaxy. *Monthly Notices of the Royal Astronomical Society*, **2004**, 354(4): L66–L72.
- [32] Ester, M., Kriegel, H.-P., Sander, J., Xu, X. A density-based algorithm for discovering clusters in large spatial databases with noise. In: Proceedings of the 2nd International Conference on Knowledge Discovery and Data Mining, Portland, Oregon, USA, **1996**: 226–231.

- [33] Schubert, E., Sander, J., Ester, M., Kriegel, H. P., Xu, X. W. DBSCAN revisited, revisited: Why and how you should (still) use DBSCAN. *ACM Transactions on Database Systems*, **2017**, 42(3): 19.
- [34] Fix, E., Hodges, J. L. Discriminatory analysis—nonparametric discrimination: Consistency properties. *Revue Internationale De Statistique*, **1989**, 57(3): 238.
- [35] Lloyd, S. Least squares quantization in PCM. *IEEE Transactions on Information Theory*, **1982**, 28(2): 129–137.
- [36] Comaniciu, D., Meer, P. Mean shift: A robust approach toward feature space analysis. *IEEE Transactions on Pattern Analysis and Machine Intelligence*, **2002**, 24(5): 603–619.
- [37] Karami, A., Johansson, R. Choosing DBSCAN parameters automatically using differential evolution. *International Journal of Computer Applications*, **2014**, 91(7): 1–11.
- [38] Martins, C., Galetti, P. M. Jr. Chromosomal localization of 5S rDNA genes in Leporinus fish (Anostomidae, Characiformes). *Chromosome Research*, **1999**, 7(5): 363–367.
- [39] Hinz, G., Chen, G., Aafaque, M., Röhrbein, F., Conradt, J., Bing, Z. S., Qu, Z. N., Stechelé, W., Knoll, A. Online multi-object tracking-by-clustering for intelligent transportation system with neuromorphic vision sensor. In: *KI 2017: Advances in Artificial Intelligence. Lecture Notes in Computer Science, Vol. 10505*. Kern-Isbener, G., Fürnkranz, J., Thimm, M., Eds. Springer Cham, **2017**: 142–154.
- [40] Chen, G. A., Cao, H., Aafaque, M., Chen, J. N., Ye, C. B., Röhrbein, F., Conradt, J., Chen, K., Bing, Z. S., Liu, X. B., et al. Neuromorphic vision based multivehicle detection and tracking for intelligent transportation system. *Journal of Advanced Transportation*, **2018**, 2018: 4815383.
- [41] Soille, P. Constrained connectivity for hierarchical image partitioning and simplification. *IEEE Transactions on Pattern Analysis and Machine Intelligence*, **2008**, 30(7): 1132–1145.
- [42] Pier, J. R., Munn, J. A., Hindsley, R. B., Hennessy, G. S., Kent, S. M., Lupton, R. H., Ivezić, Ž. Astrometric calibration of the Sloan digital sky survey. *The Astronomical Journal*, **2003**, 125(3): 1559–1579.
- [43] Lang, D., Hogg, D. W., Mierle, K., Blanton, M., Roweis, S. Astrometry.net: Blind astrometric calibration of arbitrary astronomical images. *The Astronomical Journal*, **2010**, 139(5): 1782–1800.
- [44] Dubrofsky, E. Homography estimation. Master Thesis. Vancouver, Canada: Univerzita Britské Kolumbie, **2009**.
- [45] Seedahmed, G. H. Direct retrieval of exterior orientation parameters using a 2D projective transformation. *The Photogrammetric Record*, **2006**, 21(115): 211–231.
- [46] Tsai, R. A versatile camera calibration technique for high-accuracy 3D machine vision metrology using off-the-shelf TV cameras and lenses. *IEEE Journal on Robotics and Automation*, **1987**, 3(4): 323–344.
- [47] Wijnholds, S. J., Chiarucci, S. Blind calibration of phased arrays using sparsity constraints on the signal model. In: Proceedings of the 2016 24th European Signal Processing Conference, **2016**: 270–274.
- [48] Gaia, C., Brown, A., Vallenari, A., Prusti, T., De Bruijne, J., Babusiaux, C., Juhász, Á., Marschalkó, G., Marton, G., Molnár, L., et al. Gaia Data Release 2 Summary of the contents and survey properties. *Astronomy & Astrophysics*, **2018**, 616(1): A1.
- [49] Finateu, T., Niwa, A., Matolin, D., Tsuchimoto, K., Mascheroni, A., Reynaud, E., Mostafalu, P., Brady, F., Chotard, L., LeGoff, F., et al. 5.10 A 1280 × 720 back-illuminated stacked temporal contrast event-based vision sensor with 4.86 μm pixels, 1.066 GEPS readout, programmable event-rate controller and compressive data-formatting pipeline. In: Proceedings of the 2020 IEEE International Solid-State Circuits Conference, **2020**: 112–114.



**Nicholas Owen Ralph** received his B.Eng. (Hons.) degree in mechatronics in 2017, his M.Res. degree in engineering in 2019, and has submitted his Ph.D. thesis in neuromorphic engineering. He is currently a postdoctoral research fellow in neuromorphic space imaging at the International Center for Neuromorphic Systems, MARCS Institute for Brain, Behavior, and Development at Western Sydney University, Australia. He is focusing on the development of neuromorphic approaches to space-domain awareness, astronomy, and machine learning. E-mail: N.Ralph@westernsydney.edu.au



**Alexandre Marcireau** received his M.Sc. (Eng.) degree in computer science from École Centrale, France, in 2015 and his Ph.D. degree in neuromorphic engineering from Sorbonne Université, France, in 2019. He is currently a postdoctoral research fellow in neuromorphic engineering and space applications at the International Center for Neuromorphic Systems (ICNS), Western Sydney University, Australia. His research focuses on bioinspired computer vision, event vision sensors, event-based processing, and software development. E-mail: A. Marcireau@westernsydney.edu.cn



**Saeed Afshar** completed his B.Sc. (Eng.) degree in 2014 and M.Sc. (Eng.) degree in 2016 at the University of New South Wales, Australia, and his Ph.D. degree in neuromorphic engineering at Western Sydney University, Australia, in 2020. His research focuses on the investigation of computational architectures and algorithms in the fields of neuroscience, machine learning, signal processing, and circuit design for developing novel vision, memory, and auditory sensing and processing systems with superior performance in dynamic noisy environments compared with state-of-the-art conventional computing approaches. E-mail: S.Afshar@westernsydney.edu.au



**Nickolas Tothill** majored in natural sciences at Cambridge University. He received his M.Sc. degree in radioastronomy from the University of Manchester, UK, in 1995 and his Ph.D. degree in astrophysics from the University of London, UK, in 1999. He has held research positions in Antarctica, Australia, Canada, Germany, USA, and UK. He is currently a senior lecturer in the School of Science, Western Sydney University, Australia, where he teaches physics and astronomy. His research interests include radio-astronomical surveys of the interstellar medium of the Milky Way galaxy and novel optical instruments for small telescopes, including polarimetry and event-based sensing. E-mail: N.Tothill@westernsydney.edu.au



**André van Schaik** received his M.Sc. degree in electrical engineering from the University of Twente, Enschede, the Netherlands, in 1990 and his Ph.D. degree in electrical engineering from the Swiss Federal Institute of Technology (EPFL), Lausanne, Switzerland, in 1998. He has authored over 300 publications, obtained over 35 patents, and is the founder of three start-up companies

(VAST Audio, Personal Audio, and Heard Systems). E-mail: A.vanSchaik@westernsydney.edu.au



**Gregory Cohen** received his B.Sc. (Eng.) degree in electrical and computer engineering, M.Sc. (Eng.) and B.Com. (Hons.) degrees in finance and portfolio management from the University of Cape Town, South Africa, in 2007, 2008, and 2010, respectively. He received a joint Ph.D. degree in signal processing and neuromorphic engineering from Western Sydney University, Australia, and the University of Pierre and Marie Curie in Paris, France. Prior to returning to industry research, he worked in several start-ups and established engineering and consulting firms including as a consulting engineer in the field of large-scale HVAC from 2007 to 2009, an electronic design engineer from 2009 to 2011, and an expert consultant for the Kaiser Economic Development Practice in 2012. He is currently an associate professor in neuromorphic systems at the International Centre for Neuromorphic Systems at Western Sydney University and a program lead for neuromorphic algorithms and space applications. E-mail: G.Cohen@westernsydney.edu.au

**Open Access** This article is licensed under a Creative Commons Attribution 4.0 International License, which permits use, sharing, adaptation, distribution and reproduction in any medium or format, as long as you give appropriate credit to the original author(s) and the source, provide a link to the Creative Commons licence, and indicate if changes were made.

The images or other third party material in this article are included in the article's Creative Commons licence, unless indicated otherwise in a credit line to the material. If material is not included in the article's Creative Commons licence and your intended use is not permitted by statutory regulation or exceeds the permitted use, you will need to obtain permission directly from the copyright holder.

To view a copy of this licence, visit <http://creativecommons.org/licenses/by/4.0/>.



清华大学出版社  
Tsinghua University Press



Springer